

A detailed chemical study of the extreme velocity stars in the galaxy

Tyler Nelson¹   Keith Hawkins¹   Henrique Reggiani,³ Diego Garza¹   Rosemary F.G. Wyse¹   and Turner Woody⁶

¹Department of Physics, University of Southern Maine, 96 Falmouth Street, Portland, ME 04103, USA

²Department of Astronomy, The University of Texas at Austin, 2515 Speedway Boulevard, Austin, TX 78712, USA

³ Gemini Observatory/NSF's NOIRLab, Casilla 603, La Serena, Chile

⁴Department of Astronomy and Astrophysics, The University of California at Santa Cruz, 1156 High Street, Santa Cruz, CA 95064, USA

⁵Physics and Astronomy Department, Johns Hopkins University, 3400 North Charles Street, Baltimore, MD 21218, USA

⁶Center for Astrophysics | Harvard & Smithsonian, Cambridge, MA 02138, USA

Accepted 2024 June 27. Received 2024 May 21; in original form 2023 September 29

ABSTRACT

Two decades on, the study of hypervelocity stars is still in its infancy. These stars can provide novel constraints on the total mass of the Galaxy and its dark matter distribution. However how these stars are accelerated to such high velocities is unclear. Various proposed production mechanisms for these stars can be distinguished using chemo-dynamic tagging. The advent of *Gaia* and other large surveys have provided hundreds of candidate hyper velocity objects to target for ground-based high-resolution follow-up observations. We conduct high-resolution spectroscopic follow-up observations of 16 candidate late-type hyper velocity stars using the Apache Point Observatory and the McDonald Observatory. We derive atmospheric parameters and chemical abundances for these stars. We measure up to 22 elements, including the following nucleosynthetic families: α (Mg, Si, Ca, and Ti), light/odd-Z (Na, Al, V, Cu, and Sc), Fe-peak (Fe, Cr, Mn, Co, Ni, and Zn), and neutron capture (Sr, Y, Zr, Ba, La, Nd, and Eu). Our kinematic analysis shows one candidate is unbound, two are marginally bound, and the remainder are bound to the Galaxy. Finally, for the three unbound or marginally bound stars, we perform orbit integration to locate possible globular cluster or dwarf galaxy progenitors. We do not find any likely candidate systems for these stars and conclude that the unbound stars are likely from the the stellar halo, in agreement with the chemical results. The remaining bound stars are all chemically consistent with the stellar halo as well.

Key words: stars: abundances – stars: kinematics and dynamics – stars: late-type

1 INTRODUCTION

High-velocity (HiVel) stars are unique dynamical probes for understanding the Galaxy (e.g. Hawkins et al. 2015a). Gravitationally bound HiVel stars can be used to constrain the total mass and local escape velocity of the Galaxy (e.g. Piffl et al. 2014; Williams et al. 2017). Unbound HiVel stars can be used to study the the Galaxy's dark matter halo (e.g. Gnedin et al. 2005; Gallo et al. 2022). The acceleration mechanisms for these unbound HiVel stars remains unclear (see e.g. Tutukov & Fedorova 2009; Brown 2015, and references therein).

Unbound HiVel stars, which we will refer to as hyper velocity stars¹ (HVSs), were first proposed by Hills (1988) with a more narrow usage. Hills (1988) defined HVSs as unbound stars moving on

radial orbits from the Galactic Centre (GC), potentially having galactocentric rest-frame velocities $v_{\text{GRF}} > 1000 \text{ km s}^{-1}$. They argued these stars were the product of a three-body encounter consisting of a stellar binary and a supermassive black hole (SMBH). This production pathway is the so-called Hills' mechanism. However, there are myriad potential origins for HVSs stars because of the broad definition we adopt, including accreted systems (Reggiani et al. 2022), the stellar disc, and the stellar halo, among others (see e.g. Quispe-Huaynasi et al. 2022, and references therein). HVSs can constrain the total mass of the Galaxy (Rossi et al. 2017), and the environment at the GC (Kenyon et al. 2008; Brown 2015; Rossi et al. 2017; Marchetti, Evans & Rossi 2022). Furthermore, some models for HVS production from the Large Magellanic Cloud (LMC) provide indirect evidence for the existence of either a massive black hole (Edelmann et al. 2005; Boubert & Evans 2016) or an intermediate-mass black hole (Gualandris & Portegies Zwart 2007) at the centre of the LMC.

Brown et al. (2005) provided the first observational evidence for the Hills' mechanism. They observed a B-type star (labelled HVS1) with $v_{\text{GRF}} \sim 673 \text{ km s}^{-1}$ and a galactocentric distance of 107 kpc (Brown, Geller & Kenyon 2014). This is often claimed to be the first HVS observed; however, this depends on the definition of HVS being used. This serendipitous discovery and the numerous large-

* E-mail: tyler.w.nelson@maine.edu

¹This definition is agnostic of production mechanisms for the unbound stars. Some authors use HVS to label objects from the Hills mechanism, and runaway/hyper-runaway stars for other fast-moving stars not produced in this manner. Under this alternative definition, there is then a discussion of bound and unbound HVSs. Other authors have adopted HiVel and extreme velocity to be agnostic to the origin/production mechanisms.

scale surveys of the Milky Way's (MW) stellar populations, for example, the Radial Velocity Experiment (RAVE, Steinmetz et al. 2006), the Apache Point Observatory Galactic Evolution Experiment (Majewski et al. 2017), the Sloan Digital Sky Survey (SDSS, York et al. 2000), and *Gaia* (Gaia Collaboration 2018), have caused dramatic growth in the study of HiVel stars. Much of this investigation is focused on HVSs (reviewed in Brown 2015), with less attention paid to the bound stars. However, recent works have shed light on these bounded stars as well (e.g. Hawkins et al. 2015a; Hawkins & Wyse 2018; Quispe-Huaynasi et al. 2022; Reggiani et al. 2022).

The Hills' mechanism alone cannot explain all the unbound stars observed in the Galaxy. Heber et al. (2008) showed that the B-type star HD 271791 could not have originated from the GC because its flight time would be at least twice the lifespan of the star. In addition, the apparent clumping of early type HVSs around the constellation Leo (Brown et al. 2014; Brown 2015) does not agree with the expectation that HVSs from the Hills' mechanism should be isotropically distributed around the GC. Hence, competing ideas on production emerged. In addition, there were variations on the Hills' mechanism which could produce HVS (e.g. a star interacting with a massive black hole binary, Yu & Tremaine 2003). Runaway stars are one such idea, where the observed star was jettisoned from its birth star cluster and accelerated to HiVels. This could be accomplished through dynamical evolution in clusters (Poveda, Ruiz & Allen 1967), binary interactions (Leonard & Duncan 1988) or binary supernova (SN) explosion (Blauuw 1961). Another possibility is the so-called double-degenerate double detonation scenario, where two white dwarfs orbit each other, the primary star undergoes a helium shell detonation and a subsequent carbon core detonation in a type 1a SN. Afterwards, the secondary white dwarf is accelerated to HiVel from the resulting explosion. This mechanism has been suggested for three HVS white dwarfs observed by Shen et al. (2018) and six HVS white dwarfs observed by El-Badry et al. (2023). Other origins include tidal stripping of globular clusters (Capuzzo-Dolcetta & Fragione 2015), satellite dwarf galaxies (e.g. Pereira et al. 2012; Boubert & Evans 2016), or merging galaxies (e.g. Abadi, Navarro & Steinmetz 2009; Pereira et al. 2012; Helmi et al. 2018). These HiVel stars could also originate in the stellar halo and be subsequently dynamically heated through a merger event. We refer the reader to Tutukov & Fedorova (2009) and Brown (2015), and references therein, for a more comprehensive list of possible acceleration mechanisms. Even more production pathways exist for bound HiVel stars because the energies required are less extreme compared to the unbound stars. These production pathways for HVSs are often difficult to distinguish from one another entirely; however, some progress can be made studying the possible origins of observed HVSs and their spatial distributions across the Galaxy (Brown 2015; Hawkins & Wyse 2018).

The small sample size of confirmed HVSs is a fundamental barrier to both disentangling the plethora of formation pathways proposed for these stars and their application to study the Galaxy. The small sample is both a property of their intrinsic rarity and our ability to detect these stars. The review by Brown (2015) estimates the sample size of confirmed HVS is ~ 20 based on prior literature. Distinguishing production mechanisms on the basis of ejection velocity would require 50–100 (Sesana, Haardt & Madau 2007; Perets et al. 2009) HVSs. Applications of HVSs also can require much larger samples (e.g. Gallo et al. 2022, requires up to 800 HVSs to constrain the DM halo shape). Many studies have produced candidate HVSs following the discovery in Brown et al. (2005). Boubert et al. (2018) compiled a catalogue of HVS candidates in the literature, finding over 500. Boubert et al. (2018) re-examined this catalogue of candidates using

Gaia DR2 measurements whenever possible, because of the uniform treatment of data and the improvements in astrometric precision, finding $N \sim 40$ had a probability of being bound to the Galaxy below 50 per cent. This sample only had 1 late-type star² present. A slew of new HVS candidates have been discovered following *Gaia* DR2 and DR3 (e.g. Bromley et al. 2018; Hattori et al. 2018; Marchetti, Rossi & Brown 2019; Li et al. 2021; Marchetti 2021; Raddi et al. 2021; Igoshev, Perets & Hallakoun 2023), the majority of which are oriented towards either late-type stars or white dwarfs, which had not been readily sampled before *Gaia* DR2 (see e.g. Boubert et al. 2018). These developments in turn have spurred interest in characterizing these candidate HVSs and other HiVel stars (e.g. Hawkins & Wyse 2018; Quispe-Huaynasi et al. 2022; Reggiani et al. 2022). These studies use chemo-dynamic approaches to constrain the origins of these candidate HVSs. Regardless of whether the objects are truly bound or not, constraining the origin of the sample of HVS candidates is interesting because of the diverse range of phenomena that can produce these HiVel stars. Hawkins & Wyse (2018) find their sample is comprised of halo stars, while Reggiani et al. (2022) and Quispe-Huaynasi et al. (2022) find large fractions (~ 50 per cent and ~ 86 per cent, respectively) of their samples are consistent with an accreted origin.

This study aims to expand the number of well characterized extreme velocity stars using candidates from the literature, in a similar vein as Hawkins & Wyse (2018) and Reggiani et al. (2022). We set out to take ground based observations of 16 candidate HVSs to more precisely constrain their radial velocities (RVs). We then chemically characterize them so that we may place constraints on their likely origin. This chemical characterization has seen success in Hawkins & Wyse (2018) and Reggiani et al. (2022). With our sample of 16 stars, we substantially enlarge the pool of extreme velocity stars with chemical abundances. In Section 2.1, we summarize our target selection. Section 2.2 details the data acquisition and reduction. Our methods for measuring the atmospheric parameters and chemical abundances are provided in Sections 3 and 4, respectively. A description of the kinematic analysis is given in Section 5. The results are presented in Section 6 and discussed in Section 7. Finally, a summary is given in Section 8.

2 DATA PROPERTIES

2.1 Target selection

The goal of this work is to constrain the origins and production mechanisms for these HVS candidates. In order to achieve this goal, we start by selecting HVSs to follow up from various existing literature sources (Bromley et al. 2018; Hattori et al. 2018; Marchetti et al. 2019), and from Astronomical Data Query Language (ADQL) queries by the authors using *Gaia* DR2/DR3 data shown in Appendix A. Each method uses different selection criteria therefore we will summarize each. For brevity, we omit the various quality cuts imposed by each study and encourage the interested reader to see the original work for more details.

Bromley et al. (2018) and Marchetti et al. (2019) used 3D velocities and orbit integration with an MW gravitational potential. The two studies differ in selection criteria and the masses used for the MW potential (we refer the reader to section 2.5 of Bromley et al. 2018, for more details on the differences between the works) and consequently may find different HVS candidates. Kenyon et al. (2018) have found

²That is, spectral-type FGKM.

radial and tangential velocities can be used in lieu of full 3D velocities as a reliable method for finding HVSs depending on the star's distance from the Sun. Tangential velocities are more useful for nearby stars (i.e. $\lesssim 10$ kpc from the Sun) because of the lower uncertainties in parallax, while RVs are useful at further distances. Hattori et al. (2018) find 30 candidate HVSs within 10 kpc from the Sun using only the tangential velocities. Hattori et al. (2018) note that their approach is complementary with Marchetti et al. (2019), as they use different quality cuts on the astrometric data, allowing them to potentially sample a different group of stars. Finally, we have found candidates based on galactocentric RVs from *Gaia* DR3 data. The coordinate system transformations were done using equation (1) from Hawkins et al. (2015a).

2.2 Follow-up observations

The final target selection consisted of 16 late-type HVS candidates predominately in the northern hemisphere. This sample complements the data from Reggiani et al. (2022), who used a similar sample size of candidate HVSs in the southern hemisphere to study said stars' chemistry. In addition to the program stars, we observe stars from the Gaia Benchmark catalogue (Jofré et al. 2014; Blanco-Cuaresma et al. 2014a; Heiter et al. 2015) and Bensby, Feltzing & Oey (2014) catalogue. These standard stars assist in refining the data reduction, verifying the data analysis, and calibrating derived abundances. Lastly, we re-analyse some data from Hawkins & Wyse (2018) and Reggiani et al. (2022) to assess the impact of methodological differences between the studies.

High-resolution spectra were collected using two instruments: the ARC Echelle Spectrograph (ARCES) on the 3.5-m Apache Point Observatory Telescope (Wang et al. 2003), and the Tull Echelle Spectrograph (TS, Tull et al. 1995) on the 2.7-m Harlan J. Smith Telescope (HJST) at the McDonald Observatory. ARCES observations completely sample 3800 – 9200 Å with a resolving power $R = \lambda/\Delta\lambda \sim 31\,500$. TS observations used slit 4 with a resolving power of $\sim 60\,000$ and a wavelength coverage of $\sim 3500 – 10000$ Å with interorder gaps towards the redder wavelengths. For both instruments, standard calibration exposures were also obtained (i.e. biases, flats, and ThAr lamp). Raw data were reduced in the usual fashion (i.e. bias removal, flat-fielding, cosmic ray removal, scattered light subtraction, optimal extraction, and wavelength calibration) using PYRAF/IRAF.³

To normalize the spectra, we fit a pseudo-continuum using cubic splines and iterative sigma clipping. Orders are then combined using a flux weighted average. We discard 50 pixels on either end of each order because of the poor signal due to the blaze function. We compared the normalization of the Gaia Benchmark stars we observed to a reference normalization (Blanco-Cuaresma et al. 2014a) to fine tune the sigma-clipping parameters. The signal-to-noise ratio (SNR) was estimated at the end of the normalization and order stitching by calculating the standard deviation in the normalized flux with values between 1 and 1.2 over a 60 Å window,⁴ in the middle of the chip at 5200 Å. Assuming Gaussian noise, we can transform

³IRAF is distributed by the National Optical Astronomy Observatory, which is operated by the Association of Universities for Research in Astronomy (AURA) under a cooperative agreement with the National Science Foundation.

⁴The width of the wavelength window is roughly half the wavelength range of an order and therefore gives a middle ground as to the quality of data on average.

this into a robust estimate for the true noise using a half-normal distribution.⁵ The upper limit on the flux mitigates the impact of hot pixels and cosmic rays,⁶ while the lower limit avoids confusing absorption features with noise. Our median SNR over the range 5170 – 5230 Å was 28 pixel⁻¹ for ARCES, and 32 pixel⁻¹ for TS. ISPEC (Blanco-Cuaresma et al. 2014b) was used to perform the final bad pixel removal,⁷ RV and the barycentric corrections. The RV was determined using a cross correlation with an atomic line list. These results agreed very well with the *Gaia* DR3 RVs. The barycentric corrections were found using the built in ISPEC calculator. A summary of the observational parameters can be found in Table 1. Data from Hawkins & Wyse (2018) and Reggiani et al. (2022) were processed in an identical manner.

Two targets, Star 1 (*Gaia* DR3 source id 1400950785006036224) and Star 6 (*Gaia* DR3 source id 1042515801147259008) were observed with both ARCES and TS providing a check on the validity of our reduction method.

The initial sample had a contaminant (*Gaia* DR3 source id 4150939038071816320). We believe this was from problems with the observed spectrum from the first version of *Gaia* DR2 leading to an erroneously large RV measurement, with $|V_r| > 500$ km s⁻¹. Our RV measurements indicate this is not an extreme velocity star, $V_r \sim -21.6 \pm 1$ km s⁻¹ which agrees with the *Gaia* DR3 estimate of $V_r \sim -22.3 \pm 3.9$ km s⁻¹, with a total velocity similar to the Sun. We conclude that it is not an extreme velocity star and is omitted from our data tables. It was processed in the same manner as the science sample and provides another check on our methodology. We compared our RV measurements with the estimates from *Gaia* in Fig. 1. We find good agreement between the *Gaia* DR2 estimates and our measurements, with the *Gaia* measurements being on average 7.5 km s⁻¹ larger than the values we measured from our follow-up observations.

2.3 External data

We use external data for our targets to aid in the isochrone analysis in Section 3.2 and the kinematic analysis in Section 5. We use astrometric data from *Gaia* DR3 (Gaia Collaboration 2021). Rather than using parallax to estimate distance, we use the distance estimates from Bailer-Jones et al. (2021) because more than a third of our stars have relative parallax errors greater than 10 per cent.

We use the following photometric data (when available):

- (i) *Gaia* DR2 *G*-band magnitude (Gaia Collaboration 2016, 2018; Evans et al. 2018).
- (ii) 2MASS (Two Micron All Sky Survey) *J*, *H*, *K_s* bands and associated uncertainties (Skrutskie et al. 2006).
- (iii) AllWISE *W1*, and *W2* bands and associated uncertainties (Wright et al. 2010).
- (iv) SkyMapper *u*, *v*, *g*, *r*, *i*, *z* bands and associated uncertainties (Wolf et al. 2018).

⁵The choice of a half-normal distribution was motivated by the relative ease to measure noise above the continuum, compared to below the continuum where absorption features must be contended with.

⁶The choice of an upper limit to remove spurious large flux values could inflate the SNR. In practice, the influence of this choice only changes the SNR by a few for most stars.

⁷To remove the influence of hot pixels we masked that data out and inflated the errors on the points around them by a factor of 10. For dead pixels, we masked but did not inflate the errors of neighbouring data.

Table 1. The observational parameters of the stars used in this study. A complete machine-readable version is available online. The astrometry is from *Gaia* DR3. We elect to use the distances from Bailer-Jones et al. (2021) in lieu of the values from parallax inversion from *Gaia* DR3 because more than a third of our science stars have relative parallax errors greater than 10 per cent. Radial velocities are derived from the ground-based follow-up observations along with the SNR. The literature source of the candidate HVS is provided in the reference column. Stars used for calibrations or previous detailed in other studies (e.g. Hawkins & Wyse 2018; Reggiani et al. 2022) are not included in our data tables. We use the abbreviation McD to indicate the observations were taken at the McDonald Observatory, and APO for the Apache Point Observatory. The ADQL entry in the source column indicates the targets were acquired from the ADQL query listed in Appendix A.

<i>Gaia</i> DR3 source id	Alias	Observatory	RA °	Dec. °	Distance (pc)	G (mag)	RV (km s ⁻¹)	σ_{RV} (km s ⁻¹)	SNR	Reference
1400950785006036224	Star 1	McD	233.9279	46.5688	5582	13.07	49.7	0.2	28	Hattori et al. (2018)
4531575708618805376	Star 2	APO	281.8599	22.1394	6322	13.04	-420.1	0.1	28	Marchetti et al. (2019)
2629296824480015744	Star 3	APO	335.8334	-2.5197	638	11.36	-165.6	0.2	22	Hattori et al. (2018)
3784964943489710592	Star 4	APO	169.3563	-5.8154	2555	12.24	118.4	0.2	66	Marchetti et al. (2019)
1396963577886583296	Star 5	APO	237.7316	44.4357	19 923	13.23	-417.5	0.1	18	Marchetti et al. (2019)
1042515801147259008	Star 6	McD	129.7990	62.5013	2110	12.71	72.9	0.5	36	Hattori et al. (2018)
1383279090527227264	Star 7	APO	240.3373	41.1668	6311	13.00	-184.4	0.2	46	Bromley et al. (2018)
1478837543019912064	Star 8	McD	212.4777	33.7129	5805	13.08	-246.1	0.6	27	Bromley et al. (2018)
1552278116525348096	Star 9	McD	204.6690	48.1565	1603	12.66	-76.3	0.3	43	Hattori et al. (2018)
3705761936916676864	Star 10	McD	192.7642	4.9411	2836	13.18	87.8	0.2	13	Hattori et al. (2018)
4395399303719163904	Star 11	McD	258.7501	8.7314	6591	13.17	26.6	0.2	26	Marchetti et al. (2019)
1598160152636141568	Star 12	McD	234.3616	55.1622	3063	10.78	-167.3	0.2	47	Hattori et al. (2018)
4535258625890434944	Star 13	McD	278.4475	23.1167	3804	13.13	-204.4	0.6	27	Bromley et al. (2018)
2159020415489897088	Star 14	McD	273.3214	61.3187	4893	12.50	-108.5	0.6	32	Bromley et al. (2018)
3713862039077776256	Star 15	McD	206.5166	4.1533	4798	11.17	489.8	0.1	42	ADQL query
4531308286776328832	Star 16	McD	282.5286	21.6281	2582	11.83	-619.2	0.1	54	ADQL query

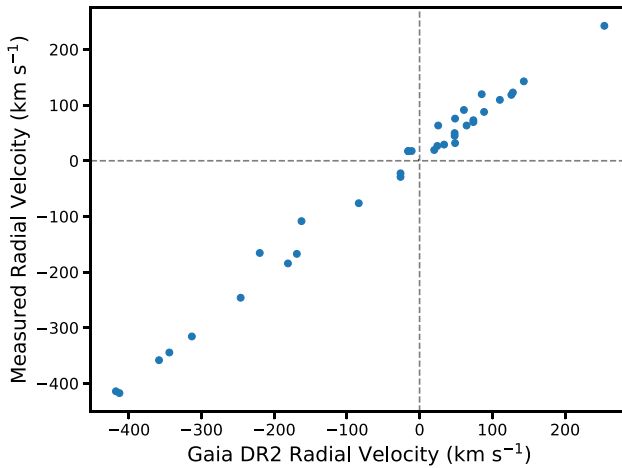


Figure 1. Displayed is a comparison of the RVs measured in this study versus those from *Gaia* DR2. Generally we find very good agreement between the two studies. Error bars are included and are smaller than the typical point size. Dashed lines indicate an RV of 0 (km s⁻¹).

(v) PANSTARRs (Panoramic Survey Telescope and Rapid Response System) *g*, *y* bands and associated uncertainties (Chambers et al. 2016; Magnier et al. 2020).

(vi) SDSS *u*, *z* bands and associated uncertainties (Blanton et al. 2017).

These bands must pass quality cuts.⁸ These cuts are identical to the recommendations put forward by each survey, with the exception of SDSS where we allowed a bad pixel within 3 pixels of the centroid,

⁸SkyMapper: [link](#)

SDSS: [link 1](#), [link 2](#)

Pan-STARRS: [link 1](#), [link 2](#), [link 3](#)

2MASS: [link 1](#), [link 2](#)

otherwise none of our stars would have usable SDSS photometry. Since the SDSS *u* band is the bluest band we use, retaining it is important for constraining the metallicity and extinction. All photometric data used in our subsequent fitting is provided in Table 2. We also use extinction estimates from BAYESTARS (Green et al. 2019).

3 ATMOSPHERIC PARAMETERS

One of the primary goals of the work is to measure the atmospheric properties (i.e. effective temperature, surface gravity, metallicity, and microturbulence) of these HVS candidates. High-quality measurements of these properties are necessary to infer chemical abundances, and thus constrain the origins and production mechanisms of these fast stars. Our spectra for the HVS candidates are low- to mid-SNR and appear metal poor based on visual inspection of the spectra. These data properties make a purely spectroscopic analysis challenging, as low SNR limits the number of weak absorption features we can use, and the metal-poor nature implies that we must be careful about non-local thermodynamic equilibrium (NLTE) effects. To achieve the highest quality atmospheric parameters, we develop a workflow that combines spectroscopic, astrometric, and photometric information simultaneously to find a self-consistent model for the star similar to section 3 of Reggiani et al. (2022); however, we choose to use a spectral synthesis approach rather than a line-by-line synthesis used in the aforementioned study due to the low SNR of our spectra. Our spectroscopic analysis is done using methods and models which assume local thermodynamic equilibrium (LTE), departures from these assumptions can arise in the metal-poor regime and may be substantial (see e.g. Frebel et al. 2013), however the photometric information is less affected by this (see e.g. Frebel et al. 2013, and references therein). The photometric data also bypasses the problems of low SNR spectra, while being sensitive to both the effective temperature (T_{eff}), and surface gravity ($\log g$). However, the photometric metallicity ([Fe/H]) signal is weaker and heavily reliant on blue bands and extinction estimates. On the other

Table 2. A portion of the photometric data used for isochrone fitting. For compactness, we only display a subset of the columns. We assume an error of 0.005 mag for the *Gaia G*-band magnitude. When values are not present or do not pass our quality cuts, a nan value is provided. The *Gaia* photometry corresponds to *Gaia* DR2 with the values from *Gaia* DR3 producing no changes. The J , σ_J , H , σ_H , K_s , σ_{K_s} correspond to the 2MASS survey. W_1 and W_2 are photometry from AllWISE. We use SkyMapper DR2 data, PANSTARRs DR1 data, and SDSS IV data when available. A full machine readable version of the table is available online.

Alias	<i>Gaia</i> DR3	<i>Gaia G</i> (mag)	J (mag)	σ_J (mag)	H (mag)	σ_H (mag)	K_s (mag)	σ_{K_s} (mag)	W_1 (mag)	σ_{W_1} (mag)	W_2 (mag)	σ_{W_2} (mag)
Star 1	1 400 950 785 006 036 224	13.073	11.53	0.02	10.91	0.02	10.88	0.01	10.79	0.02	10.84	0.02
Star 2	4 531 575 708 618 805 376	13.043	11.14	0.02	10.50	0.02	10.38	0.02	10.26	0.02	10.33	0.02
Star 3	2 629 296 824 480 015 744	11.363	9.93	0.02	9.51	0.02	9.38	0.02	9.31	0.02	9.35	0.02
Star 4	3 784 964 943 489 710 592	12.238	10.71	0.03	10.18	0.02	10.10	0.02	10.02	0.02	10.08	0.02
Star 5	1 396 963 577 886 583 296	13.229	11.13	0.02	10.36	0.02	10.19	0.02	10.11	0.02	10.19	0.02
Star 6	1 042 515 801 147 259 008	12.706	11.13	0.02	10.68	0.03	10.59	0.02	10.51	0.02	10.52	0.02
Star 7	1 383 279 090 527 227 264	12.998	11.52	0.02	10.99	0.02	10.90	0.02	10.82	0.02	10.86	0.02
Star 8	1 478 837 543 019 912 064	13.083	11.75	0.02	11.31	0.02	11.22	0.02	11.17	0.02	11.18	0.02
Star 9	1 552 278 116 525 348 096	12.664	11.52	0.02	11.14	0.03	11.11	0.02	11.04	0.02	11.07	0.02
Star 10	3 705 761 936 916 676 864	13.184	11.77	0.02	11.27	0.03	11.21	0.02	11.13	0.02	11.19	0.02
Star 11	4 395 399 303 719 163 904	13.172	11.35	0.02	10.70	0.03	10.55	0.03	10.43	0.02	10.47	0.02
Star 12	1 598 160 152 636 141 568	10.780	9.10	0.02	8.53	0.03	8.37	0.02	8.32	0.02	8.35	0.02
Star 13	4 535 258 625 890 434 944	13.126	11.60	0.02	11.11	0.03	11.02	0.02	10.96	0.02	11.00	0.02
Star 14	2 159 020 415 489 897 088	12.505	10.81	0.02	10.21	0.02	10.06	0.02	10.01	0.02	10.07	0.02
Star 15	3 713 862 039 077 776 256	11.170	9.48	0.03	8.86	0.02	8.75	0.02	8.66	0.02	8.74	0.02
Star 16	4 531 308 286 776 328 832	11.832	10.12	0.02	9.56	0.02	9.45	0.02	9.36	0.02	9.37	0.02

hand, the spectroscopic fitting is more sensitive to the metallicity and microturbulent velocity (ξ), while largely agnostic about the presence of extinction. Hence, we measure $T_{\text{eff}}/\log g$ using photometry and metallicity/ ξ from spectroscopy. We employ PYTHON code LONESTAR for the spectroscopic analysis (see Section 3.1 for details) and the PYTHON package ISOCHRONES,⁹ for the photometric analysis (see for Section 3.2 details).

The step-by-step fitting process is as follows:

- (i) Fit the spectrum with LONESTAR to find initial guesses for all atmospheric parameters (i.e. T_{eff} , $\log g$, $[\text{Fe}/\text{H}]$, and ξ).
- (ii) Fit the photometric data listed in Table 2 with ISOCHRONES using values from LONESTAR as a guess.
- (iii) Re-fit the spectrum using LONESTAR holding $T_{\text{eff}}/\log g$ fixed from the photometric fit in step 2. A guess for ξ is created using the surface gravity relationship from Kirby et al. (2009), their equation (2).
- (iv) Re-fit the photometric data using ISOCHRONES with the updated $[\text{Fe}/\text{H}]$ from the previous step, allowing all parameters to vary.
- (v) Repeat the previous two steps until the metallicity estimates from LONESTAR and ISOCHRONES converge¹⁰ or stability in the atmospheric parameters is attained

Typically it takes a couple of iterations to reach termination (i.e. the metallicity is consistent or stable in both methods). Convergence in metallicity is preferable but not always achievable. Differences of up to 0.2 in metallicity were found for some stars between the photometric and spectroscopic fits. This is in line with Bochanski et al. (2018), who find the mean spectroscopic and photometric metallicities of two clusters to be discrepant at the 0.15 dex level. Often this appeared with fits that had anomalously high extinction fits, using higher dust content to counteract higher metals. There are known shortcomings in photometric models of stars as well. In the event the two metallicity measurements do not agree within

the total errors (i.e. the internal errors added in quadrature with the external errors) we use the spectroscopic metallicity. We reason that this represents the closest approximation to the real value because spectral lines are sensitive to the bulk abundance changes the metallicity represents. Metallicity and microturbulence are also not strongly correlated for those fits. In contrast, the photometric fits for metallicity show a strong degeneracy with extinction estimates even with strong priors on the dust because our blue-band photometry does not place strong enough constraints on the isochrone fit. We found this discrepancy between the photometric and spectroscopic metallicity was also present for the test star we analysed from Reggiani et al. (2022), with a difference of ~ 0.15 dex. However, if we consider only the spectroscopic metallicity, we find the same measurement as Reggiani et al. (2022).

Internal errors for each parameter are derived from the method used to measure said parameter. T_{eff} and $\log g$ are measured using photometry and we use the posteriors from ISOCHRONES as their internal uncertainties. ξ is measured solely from spectroscopy. The internal error for ξ from the posterior was small for all stars, and we took the largest value of 0.03 km s^{-1} as the assumed error for the entire sample. As discussed below, the external errors for ξ are 2 orders of magnitude larger, so this choice does not materially change the results. Lastly, the metallicity is measured in both the photometric and spectroscopic approaches. We prefer and use the spectroscopic value because, as previously stated, we have more confidence in the accuracy of it. The internal error for the metallicity was taken as the quadrature sum of the internal errors from the photometric and spectroscopic posteriors.

To evaluate the efficacy of our atmospheric parameter estimation, we compare our fits to the literature values for the standard stars. Since this study focuses on metal-poor objects, we limit our comparison to objects with $[\text{Fe}/\text{H}] \lesssim -0.5$ dex. We find the following median offsets and dispersion $\Delta T_{\text{eff}} = 181 \text{ K}$, $\sigma_{T_{\text{eff}}} = 40 \text{ K}$, $\Delta \log g = 0.07 \text{ dex}$, $\sigma_{\log g} = 0.13 \text{ dex}$, $\Delta [\text{Fe}/\text{H}] = 0.06 \text{ dex}$, $\sigma_{[\text{Fe}/\text{H}]} = 0.04$, $\Delta \xi = 0.01 \text{ km s}^{-1}$, and $\Delta \xi = 0.28 \text{ km s}^{-1}$. The external error for each parameter is taken as the standard deviation of the difference, yielding $\sigma_{\text{ext}[\text{Fe}/\text{H}]} \sim 0.08 \text{ dex}$, $\sigma_{\text{ext}T_{\text{eff}}} \sim 40 \text{ K}$, $\sigma_{\text{ext} \log g} \sim 0.13 \text{ dex}$,

⁹<https://github.com/timothydmorton/isochnes>

¹⁰Convergence is defined as overlap in the 1σ total error intervals for the metallicity estimates from LONESTAR and ISOCHRONES.

and $\sigma_{\text{ext}_\xi} \sim 0.28 \text{ km s}^{-1}$. For the literature comparison our sample included HD 122563, which is a Gaia Benchmark star. We elected to use a microturbulence value of 1.8 km s^{-1} rather than the value of 1.13 km s^{-1} listed in Jofré et al. (2014). We calculate this revised value using the *Gaia*–ESO relationship. We prefer our revised value as the literature value seems very abnormal compared to even the paper it is listed in.

3.1 LONESTAR

LONESTAR is a PYTHON code written by T. Nelson to perform stellar atmospheric and abundance fitting for high-resolution spectra. The goal of this package was to combine the benefits of traditional synthesis-based approaches (e.g. BACCHUS, Masseron, Merle & Hawkins 2016) with a Bayesian framework to improve the error analysis and work at lower SNR. The code is organized into two modules, `abund` and `param`. The latter will be detailed here, with additional details for the abundance fitting provided in Section 4.

The user designates an interpolator, a collection of wavelength regions of interest, which atmospheric parameters should be varied, and what priors to use for the Bayesian regression. The fitter then uses the Markov Chain Monte Carlo (MCMC) PYTHON package EMCEE¹¹ to maximize the posterior probability distribution. We typically require 18–24 walkers and around 3000 iterations to converge. We attempt to account for the following sources of error when minimizing the data: flux errors, interpolator reconstruction errors, and synthesis errors. To accomplish this, we introduce an error softening term for remaining unaccounted for terms to improve performance which is simultaneously fit along with the atmospheric parameters. The following parameters can be varied or fixed: T_{eff} , $\log g$, $[\text{Fe}/\text{H}]$, ξ , and rotational broadening ($V\sin i$). $V\sin i$ is applied on-the-fly using a convolution recipe from Gray (2008), which assumes a limb darkening coefficient of $\epsilon = 0.6$. We use the wavelength sampling of ARCES for the atmospheric parameter fitting for a homogeneous analysis. This results in a downsampling of the data from TS by a factor of 2; however we have found this makes a negligible difference to the values fit for various test cases (including all stars from Nelson et al. 2021). Models are originally created with a wavelength sampling three times higher than the TS data and subsequently downsampled to the ARCES wavelength space.

The Payne (Ting et al. 2019) was used as the interpolator. We synthesized a library of $\sim 11\,000$ spectra to train this artificial neural network with a single hidden layer containing 300 nodes.¹² To create our library of synthetic spectra we randomly sampled the following intervals: $3900 \text{ K} \leq T_{\text{eff}} \leq 7000 \text{ K}$, $0 \text{ dex} \leq \log g \leq 5 \text{ dex}$, and $-3 \leq [\text{Fe}/\text{H}] \leq 1$. For each combination of T_{eff} , $\log g$, and $[\text{Fe}/\text{H}]$ we create three synthetic spectra by setting ξ equal to 0, 1.5, and 2.6 km s^{-1} . All synthetic spectra were constructed from MARCS (Model Atmospheres with a Radiative and Convective Scheme) model atmospheres (Gustafsson et al. 2008) using TURBOSPECTRUM (Plez 2012) for radiative transfer. MARCS models are calculated in 1D LTE. If the surface gravity is $\geq 3.0 \text{ dex}$, plane-parallel models are used, and spherical models otherwise. If a combination of T_{eff} , $\log g$, and $[\text{Fe}/\text{H}]$ lies between MARCs models, an interpolation is done to

create the specified model atmosphere. The atmospheric composition uses solar abundances from Grevesse, Asplund & Sauval (2007) scaled by metallicity for most elements. MARCs models use separate abundance estimates for C, N, and O (see Gustafsson et al. 2008, section 4 for more information). We assumed the same composition for C, N, and O as the models. We use *Gaia*–ESO line list version 5 (Heiter et al. 2019) for atomic transitions. The line list includes hyperfine structure splitting for Sc I, V I, Mn I, Co I, Cu I, Ba II, Eu II, La II, Pr II, Nd II, and Sm II. We also include molecular data for CH (Masseron et al. 2014), C₂, CN, OH, MgH (Masseron, private communication), SiH (Kurucz 1992), TiO, FeH, and ZrO (Pelz, private communication).

Wavelength masking is vital for an accurate atmospheric parameter fitting process because poorly modelled regions or problematic lines can alter the minimization. To begin, we limit the usable data to the range of $4500 - 6800 \text{ \AA}$. The limit on the blue side arises from a combination of reduced detector sensitivity, low source flux from our HVS candidates because we targeted late-type stars, and difficulties inherent to accurately placing the continuum in regions of dense metal absorption. This makes accurate continuum placement for metal-rich stars challenging in the blue. Hence to be uniform in our treatment of program and standard stars we exclude data below 4500 \AA . The data showed wavelength calibration issues past 8000 \AA for some stars, therefore we excluded two lines at $\sim 8500 \text{ \AA}$ from the line selection in Hawkins & Wyse (2018). With these two lines removed, the reddest line in our line selection for iron in the atmospheric parameter fitting was at $\sim 6750 \text{ \AA}$, so an upper limit of 6800 \AA was used for the synthesis. Next we exclude features from ‘bad’ pixels which can arise from the following: leftover cosmic rays,¹³ scattered light features, or dead pixels. With this cleaned spectrum, we then mask wavelengths outside the vicinity of iron lines used in previous studies on metal-poor stars by Hawkins & Wyse (2018) and Ji et al. (2020). The line core is taken as the local minimum closest in wavelength to the line data. The extent of the wavelength window around each line is determined by a first derivative test, however adopting a small $\Delta\lambda$ window of 0.5 or 1 \AA around each iron line does not change the results.

We use Bayesian regression to estimate the atmospheric parameters. Ordinary regression determines the best fit through minimizing the differences between the error weighted sum of squared residuals between the data and the model. Bayesian regression builds on this approach by including terms to represent the behaviour of the model parameters based on previous knowledge. These additional terms are called priors. We initially adopt uninformative priors (i.e. uniform distributions) on all parameters. We limit the temperature to a range of 4000–6500 K based on the spectral types of the program stars. On subsequent iterations, where we fix T_{eff} and $\log g$, we adopt Gaussian priors for $[\text{Fe}/\text{H}]$ and ξ . The mean for $[\text{Fe}/\text{H}]$ is taken as the output from ISOCHRONES. The mean for ξ is determined by inputting the ISOCHRONES surface gravity estimate into the Kirby et al. (2009) relationship. We adopt standard deviations of 0.1 dex and 0.3 km s^{-1} for $[\text{Fe}/\text{H}]$ and ξ , respectively. This choice represents our increased confidence in values of the parameters without being overly restrictive.

¹¹<https://github.com/dfm/emcee>

¹²This structure differs from the one outlined in Ting et al. (2019) because we use 1 larger network for all pixels rather than a small network for each pixel in accordance with the current release of the Payne. This network architecture allows better modeling of pixel-to-pixel covariances and therefore should be more precise.

¹³We also inflate errors nearby likely cosmic rays in case of bleeding between adjacent pixels. We use the ISPEC cosmic ray detection function with a variation threshold of 0.15. For each index flagged as a cosmic ray, we inflate flux errors by a factor of 10 for the 10 closest pixels on the red side and the 10 closest on the blue side.

Upon finishing a fit, LONESTAR writes the chain file for the MCMC, a small record of the parameter fits (including fixed and freed quantities), and some diagnostic plots to visualize how the fit performed. The best fit is the median. The upper and lower 1σ errors are the 84th and 16th percentiles, respectively.

3.2 ISOCHRONES

ISOCHRONES is a package to fit MESA Isochrones and Stellar Tracks (Dotter 2016) models using the MULTINEST wrapper PYMULTINEST (Buchner et al. 2014) to photometric data. ISOCHRONES also uses Bayesian regression for data fitting, so the user can specify initial parameter values and priors for those values. If priors are not specified, ISOCHRONES adopts default distributions, we refer the interested reader to their package documentation for these.

Following the general procedure from Reggiani et al. (2022), we input the following data: atmospheric parameters (T_{eff} , $\log g$, and $[\text{Fe}/\text{H}]$), the median photogeometric distance estimates from Bailer-Jones et al. (2021), extinction estimates from the dustmapsPYTHON wrapper for BAYESTARS (Green et al. 2019), and the photometric data for our HVS candidates described in Section 2.3. The dustmaps provided by BAYESTARS are 3D if the stars are inside the modelled volume. In cases where the star resides outside the modelled volume a 2D dustmap which integrates the modelled dustmap is used instead. All of our input quantities require error estimates. For the atmospheric parameters, we adopt 100 K, 0.5 dex, and 0.1 for T_{eff} , $\log g$, and $[\text{Fe}/\text{H}]$, respectively. We assume an error floor of 0.01 mag for σ_{A_v} computed by BAYESTARS. We adopt an error floor of 5 mmag for the photometry because it improved the fitting performance, similar to Reggiani et al. (2022).¹⁴

We adopt the default priors for all quantities aside from metallicity and distance. For metallicity, we use a uniform prior between -4 and 0.5. For distance, we use a Gaussian prior centered on the median photogeometric distance from Bailer-Jones et al. (2021) and a standard deviation which is the difference in the upper and lower 1σ errors divided by two. We restrict the extinction to a range of 0 to $A_v + \sigma_{A_v} + 0.1$, where A_v is the estimate produced from BAYESTARS, σ_{A_v} is the 1σ error estimate from BAYESTARS. The extinction in ISOCHRONES is largely constrained by blue-band photometry, however most of our HVS candidates lacked good photometry in the blue. Hence constraining the extinction to realistic values was necessary. In the absence of these tight constraints, the dust can deviate substantially from the dustmaps estimates. This deviation could be caused by imperfect models or data problems, where the dust value could compensate for these shortcomings. We note that the uncertainties derived from ISOCHRONES do not include any systematics. The fitting process only uses one set of models and the uncertainties reported are solely the posteriors from the Bayesian distributions.

4 ABUNDANCES

Once the atmospheric parameters are determined, we measure abundances for up to 22 elements with the abund module of LONESTAR. The following elements are measured¹⁵: Na, Mg, Al, Si, Ca, Sc, Ti,

¹⁴Clark et al. (2022) find an even higher error floor for photometry of 50 mmag is needed in their work with ISOCHRONES.

¹⁵We attempted to measure Li. The only star which had a detection of Li was the contaminant *Gaia* DR3 source id 4150939038071816320, which was a dwarf. The remainder of our sample were giants.

V, Cr, Mn, Fe, Co, Ni, Cu, Zn, Sr, Y, Zr, Ba, La, Nd, and Eu. This list includes members from the light/odd-Z, neutron capture, α elements, and Fe-peak nucleosynthetic families.

The LONESTARabund module synthesizes spectra at different $[\text{X}/\text{H}]$ ratios. We synthesize spectra at $[\text{X}/\text{H}] = 0, \pm 0.3, \pm 0.6$ in this fitting process. A model atmosphere is created using the best-fitting values determined from atmospheric parameter fitting. Synthetic spectra are created in the same manner as the atmospheric parameters with two exceptions. First, the spectra will have the abundance of the element of interest altered. Secondly, the spectra are created using a radiative transfer code rather than interpolation from a pre-computed grid. During the initial abundance fitting, we do not assume an α enhancement based on the metallicity in order to be agnostic to the origins of these stars. The abundances change negligibly (median($\Delta[\text{X}/\text{H}]$) < 0.02) when the average α abundances (i.e. Mg, Si, Ca, and Ti¹⁶) from the first iteration are fed into the analysis.

To measure the abundance for the species of interest, the user provides a line selection. The exact wavelength of the theoretical and observed line will primarily differ from imperfect wavelength calibration and other data reduction artefacts. Such discrepancies can be significant if uncorrected (see e.g. Jofré et al. 2017, section 4.1). We use the same line core and wing search algorithm as described for the Fe lines in Section 3.1. Then abundances for individual lines are found through χ^2 minimization between the observation and synthetic spectra.¹⁷ We estimate the 1σ uncertainties using the width of the χ^2 curve (see e.g. Coe 2009). We neither downsample nor mask pixels in this step. For each line, plots of the data and synthesis are provided for visual inspection of the fit quality. During the fit process, a line may be rejected for lack of sensitivity over the $[\text{X}/\text{H}]$ range used (i.e. no change in the χ^2 values), the automatic windowing failing, inadequate sampling of the line in the data based on the window limits, and a few other pathologies. If a line is rejected based on this automatic assessment, the line data and cause of the rejection are recorded in a tracker object. These are saved for the user to review later. For any line fit, a quality flag is created indicating if there are problems with the fit (e.g. a reduced χ^2 greater than 3 or less than 0.5). Once all lines for a species are either fit or rejected, the abundances and quality flags are tabulated and output for the user. The line list selection for all elements and all stars is given in Table 3. We use a different line selection for metal-poor stars (taken as $[\text{Fe}/\text{H}] < -0.5$) and metal-rich stars. This is primarily a caution for potential NLTE effects. In addition to modeling concerns, some lines may become measurable in the absence of dense absorption caused by higher metallicities (e.g. towards the blue end of the spectrum).

We use internal quality cuts to help filter out problematic abundance measurements from specific absorption features (e.g. Co from Star 6 due to noise). These quality cuts will vary on a line-by-line and star-by-star basis therefore the final line selection for each star may be slightly different. We require all absorption lines used for abundance determination to be at least 3σ detection, where we use a local SNR estimate with the relation from Cayrel (1988) to approximate the uncertainty in the equivalent width based on the continuum placement. We supplement our automatic quality flagging

¹⁶Ti is included here because an α enhancement in the MARCs models will include Ti.

¹⁷If no local minimum is found using the input range of $[\text{X}/\text{H}]$, the abundance range is adjusted to be centred around the abundance with the smallest χ^2 in the test value set and the fit is repeated. The smallest χ^2 value may occur on the upper or lower side of the abundance range. This process repeats up to 5 times, after which we conclude we are unable to adequately model the observation.

Table 3. A portion of our line selection for each element, its atomic properties and the absolute abundance we derive for each absorption feature. A full machine-readable version, including abundances for each star for each line, is available online. The lines used will vary between stars because of the quality checks. χ is the excitation potential in eV, $\log gf$ is the logarithm of the oscillator strength f multiplied by its statistical weight g , and $\log(\epsilon)$ is the absolute abundance (after subtracting the solar abundances) derived for this line. The solar abundances adopted are from Grevesse et al. (2007), except where described otherwise in Section 4.

Identifier	Element	λ (Å)	$\log gf$ (dex)	χ (eV)	$\log(\epsilon)$ (dex)
Star 7	Cr I	5247.56	-1.59	0.961	-7.96
Star 7	Cr I	5272.0	-0.42	3.449	-7.73
Star 7	Cr I	5296.69	-1.36	0.983	-7.87
Star 7	Cr I	5300.74	-2.0	0.983	-7.88
Star 7	Cr I	5304.18	-0.67	3.464	-7.30
Star 7	Cr I	5345.79	-0.95	1.004	-7.99
Star 7	Cr I	5348.31	-1.21	1.004	-8.02
Star 7	Cr I	5409.78	-0.67	1.03	-8.00
Star 7	Cr I	5628.64	-0.74	3.422	-7.23
Star 7	Mn I	4783.42	-0.499	2.298	-8.30

with visual inspection of all lines in our selection for 7 stars of varying atmospheric parameters and SNR.

Abundances reported are taken as the median of the lines that pass quality controls. The internal errors are estimated as the standard error (i.e. $\text{std}(\text{abundance})/\sqrt{N_{\text{lines}}}$). If only one line is present we take the uncertainty on χ^2 as the internal error. To propagate the uncertainties from the atmospheric parameters we employ a sensitivity analysis in similar fashion to Hawkins et al. (2020a) and Nelson et al. (2021). For each parameter, we perturb the best-fitting model and derive abundances for this perturbed model atmosphere. The difference between the abundances from the best fit and perturbed model is the error introduced from that parameter. These abundance errors are added in quadrature with the line-by-line statistical errors for [X/H] to determine the total error for an abundance measurement. One limitation of this process is that it does not account for covariances in uncertainties between the atmospheric parameters.

The Fe line selection between the atmospheric and abundance fitting is different. For the atmospheric parameters, we use the union of lines from Hawkins & Wyse (2018) and Ji et al. (2020) whereas the abundances only use lines from the former. The change in line selection comes from distinct goals in the `param` and `abund` analysis. The former was tasked with creating a starting point so casting a wide net was desirable. The latter was a refinement of this fitting process and so we decided to use the line list the author was more familiar with. This amounts to ~ 70 fewer lines being used for Fe in the abundance determination compared to the metallicity fit. This change, along with quality selection cuts, produces an offset between the metallicity and iron abundance of -0.03 ± 0.07 for the entire sample and -0.01 ± 0.07 if we only consider stars with metallicity below -0.5 .

NLTE corrections for Ca (Mashonkina, Korn & Przybilla 2007), Co (Bergemann, Pickering & Gehren 2010), Fe (Bergemann et al. 2012a, b), Mg (Bergemann et al. 2015, 2017), Mn (Bergemann & Gehren 2008), Si (Bergemann et al. 2013), and Ti (Bergemann 2011; Bergemann et al. 2012b) are accounted for on a line-by-line basis using online tables from MPIA. Star 5 (*Gaia* DR3 source id 1396963577886583296), lies outside the atmospheric parameter range of these published val-

ues, therefore we do not attempt to apply a correction for this star.

5 DYNAMICAL ANALYSIS

We employ a dynamic analysis to assess whether these HVS candidates to answer two questions: (1) which, if any, of the HVS candidates are unbound or marginally bound? (2) For the unbound or marginally bound objects, what systems might be progenitors for these fast moving stars?

We use the PYTHON package GALPY¹⁸ for this analysis. For each orbit, we used the RVs from our observations, the Bailer-Jones et al. (2021) photogeometric distances, with the remaining astrometry from *Gaia* DR3. In general, there was very good agreement between Bailer-Jones et al. (2021) distances and those fit from ISOCHRONES. To construct our covariance matrix, Σ , for uncertainty analysis, we use the uncertainties and covariances for the right ascension (RA), declination (Dec.), proper motion in RA (pmra), and proper motion in Dec (pmdec.) from *Gaia*, and assume the RV and Bailer-Jones et al. (2021) distances are uncorrelated. We propagate measurement uncertainties to our orbit integration and other derived kinematic quantities through Monte Carlo sampling of the multivariate normal distribution $N(\mu, \Sigma)$, where μ is the measured value for each quantity. This sampling is repeated 1000 times.

We use the MWPotential2014 (Bovy 2015) to approximate the Galactic potential. This potential uses a Navarro–Frenk–White halo with a scale length of 16 kpc (Navarro, Frenk & White 1996). A Miyamoto–Nagai potential (Miyamoto & Nagai 1975) with radial scale length of 3 kpc and vertical scale height of 280 pc is used for the disc. Finally, the bulge has a power-law density profile with an exponent of -1.8 and is exponentially tapered at 1.9 kpc. We assume current values for the solar position and kinematics as $R_0 = 8.122$ kpc, $z_0 = 20.8$ pc (GRAVITY Collaboration 2018; Bennett & Bovy 2019), and a solar motion of $(U_\odot, V_\odot, W_\odot) = (12.9, 245.6, 7.78)\text{km s}^{-1}$ (Reid & Brunthaler 2004; Drimmel & Poggio 2018; GRAVITY Collaboration 2018).

6 RESULTS

6.1 Kinematics

The kinematics of the candidate HVSs is used to determine whether these objects are gravitationally bound or unbound to the Galaxy, as well as where these stars may have been produced. This production location in turn constrains how these stars were accelerated. To access whether these candidate HVS are bound, we use their present day kinematics along with a model of the MW's gravitational potential from Williams et al. (2017). We note the MW model used in Williams et al. (2017) differs from that used in Section 5. In Fig. 2, we show total velocity (v_{total}) as a function of spherical distance from the GC (r), for our candidate HVS stars (labelled by their alias) and an MW escape velocity curve with 1σ uncertainties based on the model and uncertainties from Williams et al. (2017). We calculate v_{total} and r using the photogeometric distances from Bailer-Jones et al. (2021), our ground-based RV measurements, and the remaining astrometry from *Gaia* DR3. The uncertainty band on the Williams et al. (2017) model is created using Monte Carlo sampling of their model parameter uncertainties. From this work, we see that only star is likely unbound from the Galaxy, with Stars 5, and 8 being

¹⁸<https://github.com/jobovy/galpy>

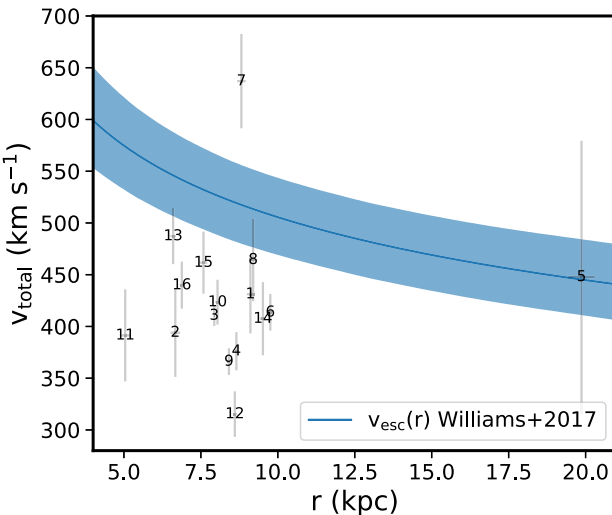


Figure 2. Displayed is the current spherical position and total velocity for each star in our sample. The numbers for each star correspond to their alias from Table 1. The error bars show the propagated uncertainties from the Monte Carlo sampling of the astrometry, RV, and distance uncertainties. The dark blue line represents the median escape velocity assuming the spherical model from Williams et al. (2017), with the contour corresponding to the 1σ range, propagating the uncertainties in parameters from Williams et al. (2017). Only Star 7 is definitely unbound, Star 5 is marginally bound, and Star 8 could be unbound based on the overlap in the error bars.

marginally unbound (1σ level). We have marked these stars in red in subsequent chemical plots to aid with their identification.

We used catalogues of globular clusters and MW satellites in GALPY to determine if there were any clear candidate progenitors for Stars 5, 7, and 8. These catalogues for globular clusters and MW satellites are based on Vasiliev (2019) and Fritz et al. (2018), respectively. We integrated these systems using a similar framework as the previous section; however, we only integrated back 300 Myr. A star travelling with 100 km s^{-1} in the radial direction would cover a distance of 30 kpc in this period, well outside the distances we expect our HVS to have travelled either from the outer Galaxy inward or vice versa. This choice also helps minimize potential inaccuracies from the uncertainty in the input phase space parameters (x, y, z, v_x, v_y, v_z) and the Galactic potential. For all systems examined, the point of closest approach for our objects is at least 10 times the the half-light radii of the candidate origin system. Doubling the integration length to 600 Myr, does not change the results. Extending the integration to 1.5 Gyr, the closest approach for Stars 7 and 8 is ~ 1 kpc from the star systems examined. Interestingly, Stars 7 and 8 share the same system of closest approach in their orbits (NGC 6205), and the same second closest system (NGC 6341). Star 5 fairs worse, with the closest approach being Draco II at 3.5 kpc, and the second closest system being NGC 6229 at ~ 8 kpc.

We conducted a second round of kinematic analysis using a modified potential. Bland-Hawthorn & Gerhard (2016) estimate a dark matter halo mass 50 per cent larger than the one used by default in MWPotential2014. In addition, GALPY is capable of modelling the impact of the LMC's gravitational potential. GALPY also provides a built in way to estimate the escape velocity from different symmetric potentials. Due to the LMC breaking cylindrical symmetry, we could only find an escape velocity estimate using the heavier dark matter halo potential. We find the escape velocity curve is unchanged from the Williams et al. (2017) model used above. The top two systems change for Star 8 and are unchanged for Stars 5 and 7. The system of

closest approach for Star 8 is NGC 5897, at a distance of ~ 280 pc roughly ~ 1.25 Gyo.

6.2 Stellar parameters and abundances

Atmospheric stellar parameters and chemical abundance measurements are displayed in Table 4. The full table includes both LTE and NLTE corrected measurements when applicable.

6.3 Comparison to prior works

As part of our analysis, we observed stars from the Gaia Benchmark stars (Jofré et al. 2014; Heiter et al. 2015) and stars from Bensby et al. (2014) to assess the differences in the atmospheric and abundance fits. We find a median offset of ~ -181 K in effective temperature. Our analysis of the stars from Hawkins & Wyse (2018) show a similar offset of ~ -187 K when compared with the previous spectroscopic temperatures. We suspect this offset arises from the discrepancy in photometric and spectroscopic temperatures. We offer two lines of evidence to support this hypothesis. First, in table 3 from Hawkins & Wyse (2018), photometric temperatures from *Gaia* DR2 are provided, which show an offset of ~ -173 K. Second, fig. 2 from Frebel et al. (2013) finds an offset of ~ -200 K between the photometric and initial spectroscopic temperatures (i.e. before NLTE considerations). Assuming we can apply the general relationship from very metal-poor objects to less metal-poor stars, this would explain the offset in temperature. Additional discussion on the impact of NLTE on effective temperature can be found in, for example, Korn, Shi & Gehren (2003) and Mucciarelli & Bonifacio (2020).

Offsets in the other atmospheric parameters are seen for the standard star sample. Comparing the atmospheric parameters for the stars in the Hawkins & Wyse (2018) sample we see $\Delta \log g = -0.9 / -0.52$ dex; $\Delta [\text{Fe}/\text{H}] = -0.44 / -0.27$ dex; and $\Delta \xi = 0.1 / -0.24 \text{ km s}^{-1}$ for the LONESTAR + ISOCHRONES/LONESTAR only fits respectively. These differences are an order of magnitude larger than those for the standard stars. These offsets could arise from differences in the treatment of NLTE, the low SNR of the data, and the fitting methods employed. Hawkins & Wyse (2018) gauge the influence of NLTE effects by redoing their fits using the photometric temperature instead, finding offsets of up to 0.3 dex in metallicity.

Abundance differences between Bensby et al. (2014); Battistini & Bensby (2015, 2016), and this study are shown in Fig. 3. Three elements lack literature comparisons: Copper (Cu), Lanthanum (La), and Europium (Eu). Copper and Lanthanum measurements were not available from the literature studies we referenced. No suitable measurements of Europium were found in our observations after filtering through our quality criteria.

There are several plausible sources for these abundance offsets; we will consider differences in atmospheric parameters and NLTE corrections. NLTE corrections do not have a consistent affect on the abundances. For Ti and Co, they increase the offset relative to a pure LTE comparison by ~ 0.1 dex, while the rest have negligible changes (i.e. $\Delta < \pm 0.05$ dex). To gauge the significance of the atmospheric parameters, we use the stars from Hawkins & Wyse (2018) as a proof of concept. After controlling for changes in bulk metallicity (i.e. using $[\text{X}/\text{Fe}]$ rather than $[\text{X}/\text{H}]$) we find comparable offsets in Mg, Si, Ca, Zn, Sr, Nd, and Y as observed in the data. Still further discrepancies could arise from the atomic data, the line selection, the visual inspection, continuum placement, and so on.

When comparing our abundance measurements to the literature abundances, we do not use NLTE corrections from Section 4 unless

Table 4. A portion of the atmospheric parameters and abundances for the HVS candidates. Stars are labelled by their alias from Table 1. The $[\text{Fe}/\text{H}]$ value is the abundance determined for iron rather than the metallicity from the atmospheric parameter fitting; however, these values are nearly identical ($|\Delta| < 0.03$). ξ is the microturbulence velocity. We only provide internal errors for T_{eff} and $\log g$ as the external errors are provided in the text and identical for each star. The internal errors for ξ (i.e. σ_{ξ}) were negligible compared to the external error therefore we do not list them. Abundances which lacked measurements are given a nan. The error in abundance measurement is the total error described in Section 4. $[\text{X}/\text{Fe}]$ values are provided in the digital version of this table. A full machine readable version of the table is available online.

Alias	T_{eff} (K)	$\sigma_{T_{\text{eff}}}$ (K)	$\log g$ (dex)	$\sigma_{\log g}$ (dex)	$[\text{Fe}/\text{H}]$ (dex)	$\sigma_{[\text{Fe}/\text{H}]}$ (dex)	ξ (km s^{-1})	$[\text{Na}/\text{H}]$ (dex)	$\sigma_{[\text{Na}/\text{H}]}$ (dex)	$[\text{Mg}/\text{H}]$ (dex)	$\sigma_{[\text{Mg}/\text{H}]}$ (dex)	$[\text{Al}/\text{H}]$ (dex)	$\sigma_{[\text{Al}/\text{H}]}$ (dex)	$[\text{Si}/\text{H}]$ (dex)	$\sigma_{[\text{Si}/\text{H}]}$ (dex)
Star 1	4654	39	1.78	0.07	-1.48	0.18	1.88	-1.45	0.24	-1.06	0.08	nan	nan	-1.10	0.04
Star 2	4588	30	1.21	0.05	-1.80	0.17	1.87	-1.82	0.12	-1.30	0.24	nan	nan	-1.50	0.06
Star 3	5158	31	3.11	0.05	-1.27	0.17	1.76	-1.29	0.24	-0.92	0.37	nan	nan	-0.94	0.05
Star 4	4763	20	2.15	0.05	-1.41	0.21	1.82	-1.20	0.23	-0.93	0.10	-1.00	0.09	-0.94	0.05
Star 5	3987	11	0.47	0.04	-1.41	0.17	1.97	-1.18	0.08	-0.79	0.20	-0.85	0.08	-0.95	0.06
Star 6	5352	56	2.47	0.02	-1.44	0.23	1.88	-1.16	0.04	-1.07	0.20	nan	nan	-1.12	0.08
Star 7	4817	13	1.74	0.06	-1.50	0.16	1.82	-1.34	0.09	-1.06	0.12	nan	nan	-1.15	0.07
Star 8	5099	47	1.93	0.09	-1.92	0.11	1.83	-1.25	0.20	-1.64	0.11	nan	nan	nan	nan
Star 9	5601	41	3.34	0.05	-1.07	0.17	1.78	-0.69	0.10	-0.63	0.04	nan	nan	-0.82	0.06
Star 10	5025	56	2.60	0.08	-1.22	0.15	1.97	nan	nan	-0.94	0.36	nan	nan	-0.85	0.12
Star 11	4469	11	1.31	0.05	-1.50	0.19	1.95	-1.34	0.16	-1.01	0.05	nan	nan	-1.09	0.06
Star 12	4526	16	1.21	0.03	-1.82	0.18	1.88	-1.80	0.07	-1.46	0.22	nan	nan	-1.56	0.05
Star 13	5048	25	2.17	0.05	-1.84	0.09	2.36	nan	nan	nan	nan	nan	nan	nan	nan
Star 14	4689	19	1.43	0.04	-2.41	0.13	1.64	nan	nan	-1.99	0.22	nan	nan	nan	nan
Star 15	4485	50	1.17	0.09	-1.50	0.22	1.87	-1.30	0.09	-1.09	0.13	-1.07	0.09	-1.12	0.07
Star 16	5023	97	1.99	0.13	-1.80	0.17	1.87	-1.78	0.08	-1.54	0.15	nan	nan	-1.41	0.20

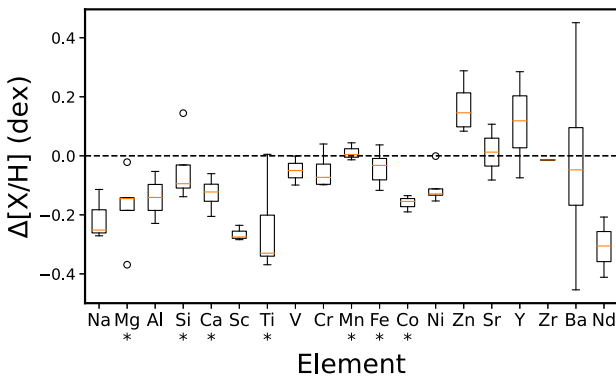


Figure 3. Differences in abundances derived for stars in Bensby et al. (2014); Battistini & Bensby (2015, 2016); and this study. Elements which use NLTE corrections in this calibration plot are marked with asterisks below their label. The disagreement between our measurements and the literature is reduced when we only examine LTE abundances and remove offsets caused by differences in metallicity measurements (i.e. use $\Delta[\text{X}/\text{Fe}]$ instead of $\Delta[\text{X}/\text{H}]$). Remaining differences are likely a consequence of differences in the T_{eff} and ξ parameters. We find differences of ~ 150 K in T_{eff} and 0.4 km s^{-1} in ξ .

otherwise specified because several of the comparison studies (e.g. Hawkins & Wyse 2018) only compute LTE abundances. In addition, we do not rescale our data based on the reference stars from Bensby et al. (2014) and Battistini & Bensby (2015, 2016) because this rescaling cannot be done uniformly for all the literature samples we compare our data with.

6.4 Literature sources

For context in Figs 4 and 5, we include measurements from studies on the thin and thick disc (Bensby et al. 2014; Battistini & Bensby 2015, 2016), the bulge (Bensby et al. 2010; Gonzalez et al. 2015), the inner halo (Nissen & Schuster 2010), metal-poor halo stars (Yong et al. 2013; Roederer et al. 2014), the LMC (Van der Swaelmen et al.

2013), and Fornax (Letarte et al. 2010). We have also included data from other studies on the chemistry of HVS/HiVel stars (Hawkins & Wyse 2018; Reggiani et al. 2022). We are comparing LTE abundances to one another in these plots.

6.5 Chemical abundances

The goal of this work is to use chemical tagging (Freeman & Bland-Hawthorn 2002) to constrain the origins of our late-type HVS candidates. Chemical evolution of the interstellar medium (ISM) is a fundamental ingredient for chemical tagging because most stellar abundances reflect the composition of their progenitor ISM. Broadly, a generation of stars will form with some initial composition. As the stars age, their interior composition will change from fusion; however, the surface composition remains roughly constant over their lifespan and hence can act as a fossil record of the progenitor system. This modified stellar composition is then dispersed into the ISM through some flavour of SN (type Ia, type II, etc.), stellar winds, or other mechanism (e.g. kilonova). The chemical evolution of the ISM depends on the availability of new materials (i.e. the amount and type of feedback) as well as the mixing efficiency of said materials with the extant gas. The type and timescales of the feedback are dependent on mass, and to a lesser extent metallicity of the stellar population (see e.g. Nomoto, Kobayashi & Tominaga 2013, and references therein).

For the first ~ 1 Gyr, massive stars are thought to be the primary contributor to the chemical evolution of the ISM owing to their relatively short lifetimes compared to low-mass stars (see e.g. Gilmore, Wyse & Kuijken 1989, section 1.3). Hence at low metallicities (e.g. $[\text{Fe}/\text{H}] \lesssim -1$ for the solar neighbourhood), the abundance patterns of the Galaxy reflect the yields from massive stars. These yields have a metallicity dependence (see e.g. Nomoto et al. 2013). After this period, feedback from lower mass stars (e.g. AGB, asymptotic giant branch winds, type Ia SN) becomes increasingly important as more low-mass stars reach the point at which they can expel their matter into the surrounding environment. Since low-mass stars are far more

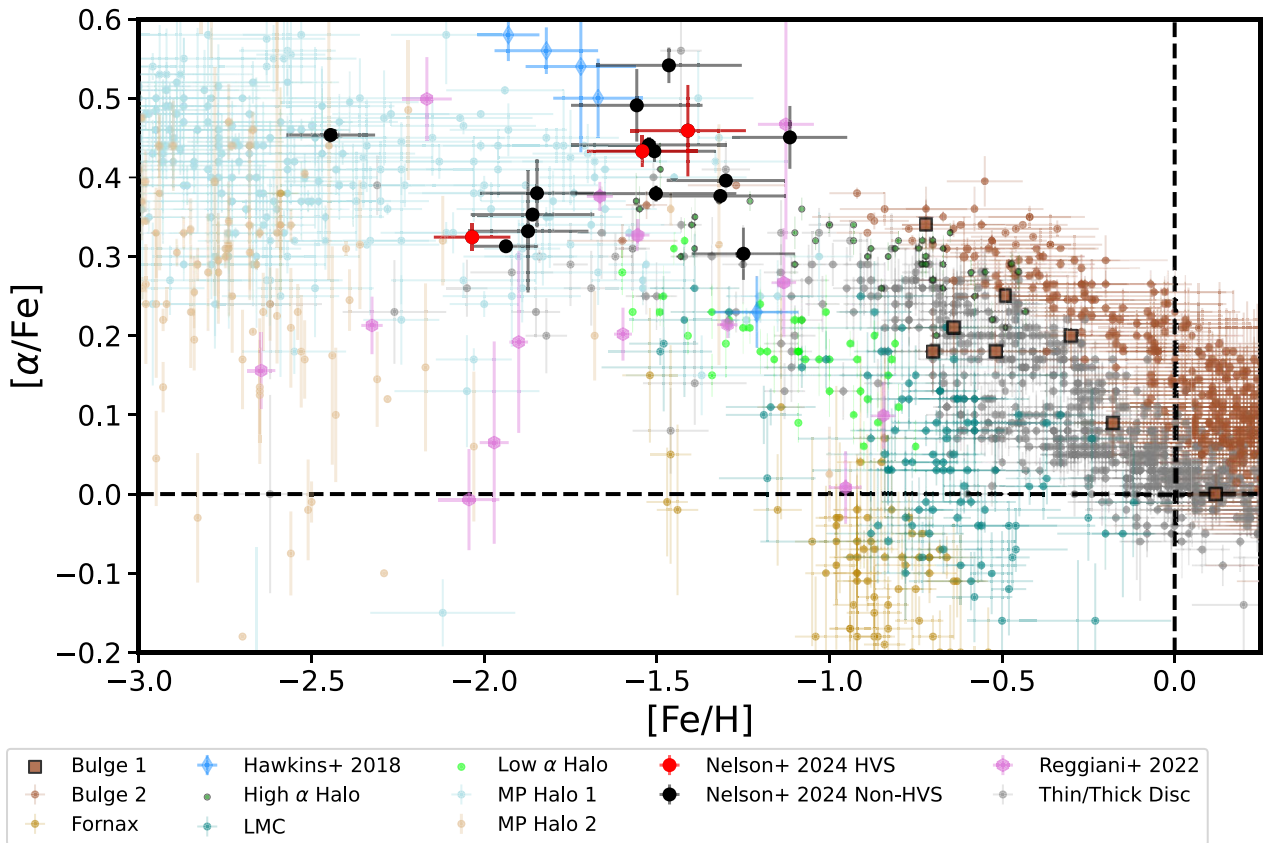


Figure 4. $[\alpha/\text{Fe}]$ abundance measurements and errors as a function of metallicity are plotted. Data points from the HVS candidates found in Section 5 are shown in red, the remainder of the sample is shown in black. $[\alpha/\text{Fe}]$ is taken as the median of $[\text{Mg}/\text{Fe}]$, $[\text{Si}/\text{Fe}]$, and $[\text{Ca}/\text{Fe}]$. If not all three elements have measurements, we take the average instead. All abundances shown are taken to be in LTE. For reference, in each panel we also show the abundance ratios of the thin and thick discs (Bensby et al. 2014; Battistini & Bensby 2015, 2016, in grey), the high α halo (Nissen & Schuster 2010, in green), the low α halo (Nissen & Schuster 2010, in bright green), the metal-poor halo (Roederer et al. 2014, in light blue; Yong et al. 2013, in tan), and the the bulge (Bensby et al. 2010; Gonzalez et al. 2015, in brown). We include abundances from two contemporary studies on the abundances of hyper velocity candidates as well, Hawkins & Wyse (2018) in blue, and Reggiani et al. (2022) in violet. Abundances for the LMC from Van der Swaelmen et al. (2013, teal) and Fornax from Letarte et al. (2010, gold) are also shown for additional context.

numerous than higher mass stars (e.g. Kroupa & Weidner 2003), eventually the feedback of materials into the ISM from the lower mass stars will tend to dominate the present-day ISM composition in areas of continuous star formation within the Galaxy. The metallicity at which low-mass stars start becoming important is dictated by the star formation rate. The total mass of star-forming matter and the initial mass function (along with the metallicity distribution function) play a similarly pivotal role in what feedback mechanisms are possible to subsequently modify the ISM.

6.6 α elements: Mg, Si, Ca, and Ti

The α elements are formed through the consecutive addition of helium nuclei (α -particles, see e.g. Burbidge et al. 1957). Titanium, while not formed in the same pathway (see e.g. Curtis et al. 2019), often follows the same trends so it is frequently included in this family of elements (see e.g. Hawkins, Lucey & Curtis 2020b). The yields from core-collapse SN (type II/Hypernova) dominate the dispersal of these elements and happen on shorter timescales than type Ia SNe. In the solar neighbourhood, this manifests as an $[\alpha/\text{Fe}]$ plateau of ~ 0.4 for $[\text{Fe}/\text{H}] \lesssim -1$. This can be seen in Fig. 4, where we have taken $[\alpha/\text{Fe}]$ as the median of the $[\text{Mg}/\text{Fe}]$, $[\text{Si}/\text{Fe}]$, and $[\text{Ca}/\text{Fe}]$ abundances measured for that star. The lower yield of α elements

compared to iron (and Fe-peak elements) present in type Ia SN causes $[\alpha/\text{Fe}]$ to decrease with increasing metallicity for $-1 \lesssim [\text{Fe}/\text{H}] \lesssim 0$ (see e.g. Lambert 1987; Wheeler, Sneden & Truran 1989; Weinberg et al. 2019). At solar metallicity, $[\alpha/\text{Fe}] \sim 0$. The inflection point at $[\text{Fe}/\text{H}] \sim -1$ is referred to as the ‘knee’. The inner halo, bulge, thin disc, and thick disc all have distinct locations in the $[\alpha/\text{Fe}]$ versus $[\text{Fe}/\text{H}]$ plane, corresponding to their evolution; however, the boundaries between the regions are not always well defined (see e.g. Feltzing & Chiba 2013; Hawkins et al. 2015b). Further, there are also signatures for accreted systems, which show a ‘knee’ at metallicities lower than -1 dex.

Results for individual α elements are shown in Fig. 5. We also show the combined abundance pattern in Fig. 4, where we have taken $[\alpha/\text{Fe}]$ as the median of the $[\text{Mg}/\text{Fe}]$, $[\text{Si}/\text{Fe}]$, and $[\text{Ca}/\text{Fe}]$ abundances measured for that star.

Overall, we find relatively good agreement between the chemical patterns of our stars and the inner stellar halo. This is consistent with the picture from Hawkins & Wyse (2018). However, we do not see a significant low α component in contrast to Quispe-Huaynasi et al. (2022) and Reggiani et al. (2022) which are both follow-up studies on the chemistry of HVS candidates. We examined all stars with $[\alpha/\text{Fe}] \lesssim 0.3$ to check if these objects were consistent with accreted origins and the so-called low α halo from Nissen & Schuster (2010).

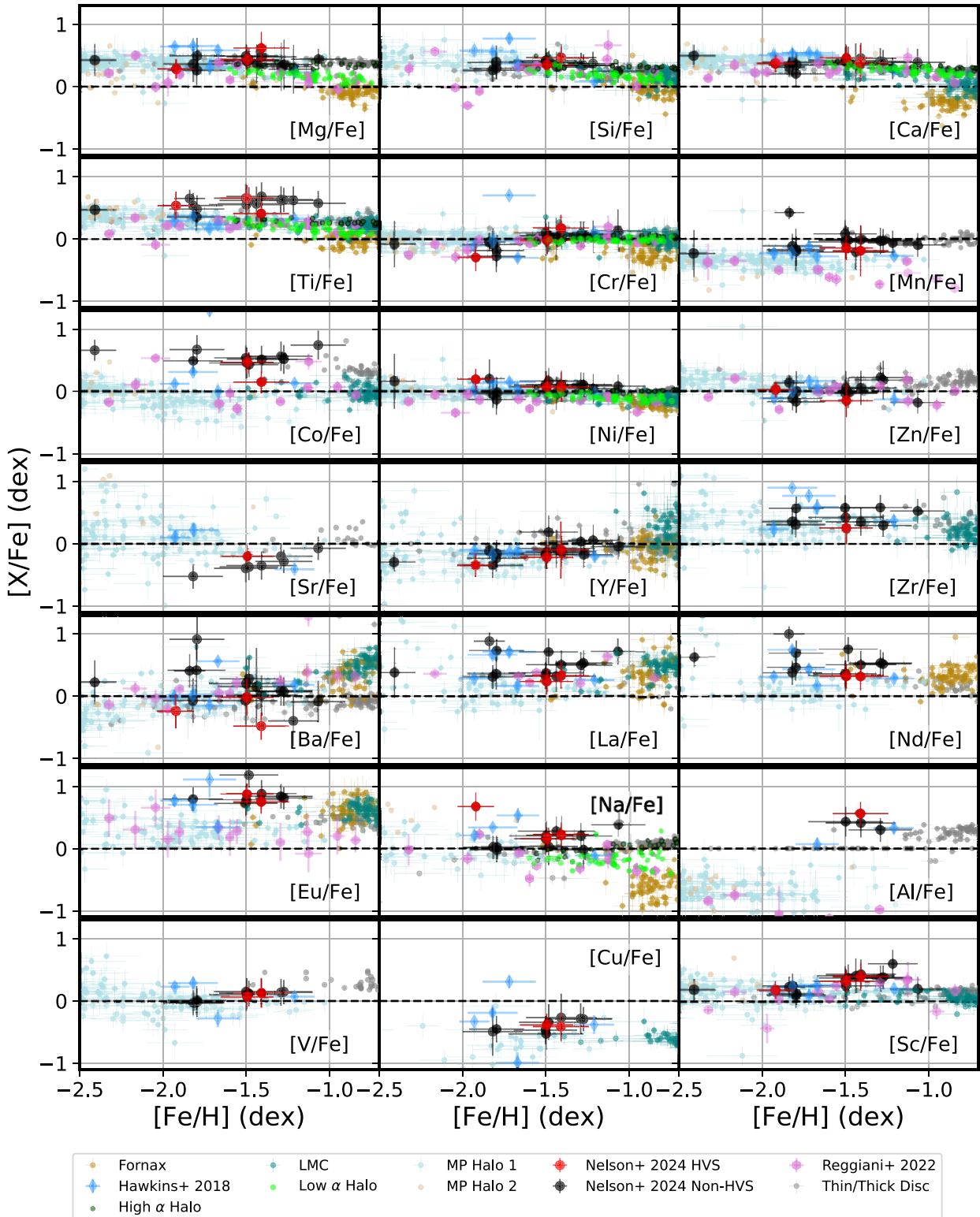


Figure 5. $[X/Fe]$ abundance measurements and errors as a function of metallicity are plotted. Data points from the HVS candidates found in Section 5 are shown in red, the remainder of the sample is shown in black. All measurements compared are in LTE. For reference, in each panel we also show the abundance ratios of the thin and thick discs (Bensby et al. 2014; Battistini & Bensby 2015, 2016, in grey), the high α halo (Nissen & Schuster 2010, in green), the low α halo (Nissen & Schuster 2010, in bright green), the metal-poor halo (Roederer et al. 2014, in light blue; Yong et al. 2013, in tan), and the the bulge (Bensby et al. 2010; Gonzalez et al. 2015, in brown). We include abundances from two contemporary studies on the abundances of hyper velocity candidates as well, Hawkins & Wyse (2018) in blue, and Reggiani et al. (2022) in violet. Abundances for the LMC from Van der Swaelmen et al. (2013, teal) and Fornax from Letarte et al. (2010, gold) are also shown for additional context.

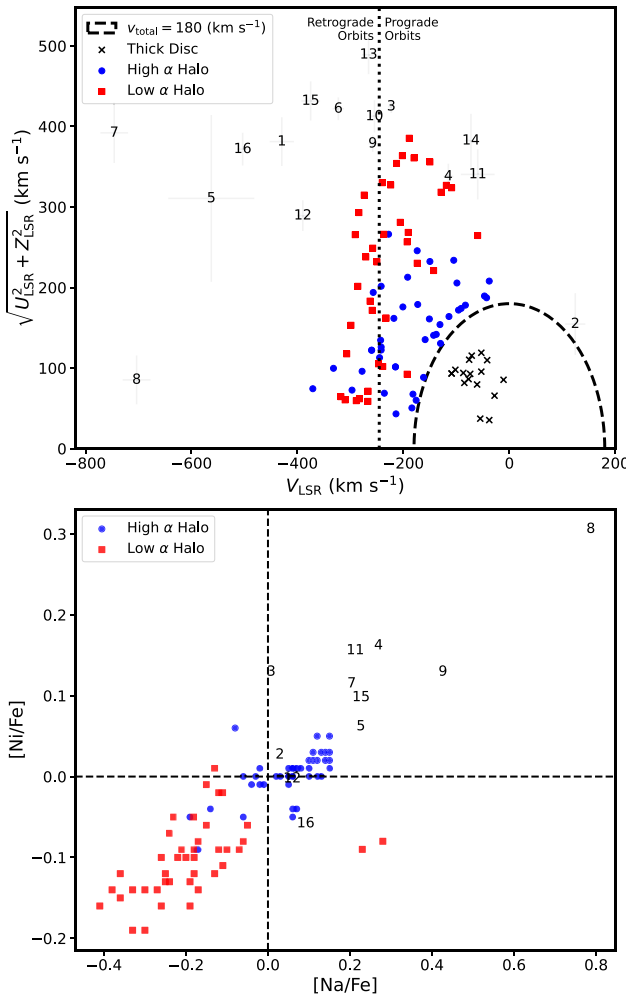


Figure 6. Top: a Toomre diagram for the HVS candidates in this paper. For ease of reference, each star in the paper is labelled by the number in its alias (i.e. Star 7 is labelled 7). Data from Nissen & Schuster (2010) is included for comparison. The high α , low α , and thick disc data from Nissen & Schuster (2010) are labelled HA (circle), LA (square), and TD, respectively (black cross). Bottom: a comparison of the [Na/Fe] and [Ni/Fe] abundances for the candidate HVSs. Aliases are used for points similar to Fig. 6. Data from Nissen & Schuster (2010) is included for comparison and labelled as in Fig. 6. The abundances used and compared to in this panel use LTE.

Nissen & Schuster (2010) show that the low and high α haloes cluster differently in Toomre space and in [Ni/Fe] versus [Na/Fe] space. The usefulness of the Toomre space clustering is hampered by our selection criteria of fast moving stars. In the Toomre space, shown in Fig. 6, our entire sample of candidate HVSs appear more consistent with the fast moving low α halo compared to the slower high α ; however, most of our sample appears chemically consistent with the high α halo. This is also found when we compare the [Ni/Fe] versus [Na/Fe], shown in Fig. 6, finding no stars which are unambiguously in the low α halo cluster.

6.7 Light/odd-Z elements: Na, Al, V, Cu, and Sc

Odd-Z elements are produced in a variety of nucleosynthetic pathways. Sodium (Na) and Aluminum (Al) can both experience strong

NLTE effects at low metallicities (see e.g. Kobayashi, Karakas & Lugaro 2020, and references therein), making their interpretation difficult. Fig. 5 displays our measurements of Na, Al, V, Cu, and Sc in [X/Fe] versus [Fe/H] space (black circles). As before, we see that our stars are consistent with the stellar halo. Unlike Reggiani et al. (2022), we do not see any evidence in [Na/Fe] of our stars being consistent with a dwarf or accreted galaxy. We find [Al/Fe] which is over 1 dex greater than other literature we compared to. This difference in [Al/Fe] might be a result of different line selection between our study and Yong et al. (2013), Roederer et al. (2014), and Reggiani et al. (2022), all of which use lines close to ~ 4000 Å, a section of data that we discarded during the reduction (see Section 3). We instead use 5557.06, 6696.02, and 6698.67 Å to measure the Aluminum abundance. These are weak lines in our program stars, so we are only able to measure Al in a handful of spectra. Applying NLTE corrections for Na does not meaningfully change the offsets between our values and Reggiani et al. (2022) for our line selection, so we conclude that most of our stars are likely not accreted or debris from a satellite galaxy.

6.8 Fe-peak elements: Cr, Mn, Co, Ni, and Zn

The Fe-peak elements are primarily synthesized with type Ia and core-collapse SNe (e.g. Nomoto et al. 2013). These elements largely trace the iron abundance. As such, most of these elements are expected to have a roughly flat trend of [X/Fe] against metallicity. We plot our results of [Cr, Mn, Co, Ni, Zn/Fe] (black circles) in Fig. 5. We find further evidence that these stars are likely from the halo based on their agreement with Nissen & Schuster (2010) and Hawkins & Wyse (2018) in [Ni/Fe] and [Cr/Fe]. Our Cobalt (Co) abundances tend to be higher than Yong et al. (2013) and Roederer et al. (2014), but are within the range seen by Hawkins & Wyse (2018) and Reggiani et al. (2022).

6.9 Neutron-capture elements: Sr, Y, Zr, Ba, La, Nd, and Eu

The neutron-capture elements are commonly split into those which are primarily produced in the slow neutron-capture process (*s*-process) and the rapid neutron-capture process (*r*-process). The *s*-process elements (Sr, Y, Zr, Ba, La, and Nd) are formed in AGB stars and then returned to the ISM through stellar winds. By contrast, *r*-process elements are formed with rapid neutron capture. The exact nature of what processes drive this is still an open area of research, with binary neutron star mergers being one such candidate (van de Voort et al. 2020). The neutron-capture element abundance ratios for our stars (black circles) for [Sr, Y, Zr, Ba, La, Nd, Eu/Fe] as a function of metallicity are shown in Fig. 5. Of the neutron-capture elements we measure, all are members of the *s*-process group except Eu. These elements are consistent with the stellar halo.

7 DISCUSSION

In our sample, we find only one star that seems unbound based on the adopted escape velocity from Williams et al. (2017). Further, there is one marginally bound star and one star which could potentially be marginally bound on the overlap in its v_{total} uncertainties and the escape velocity uncertainties.

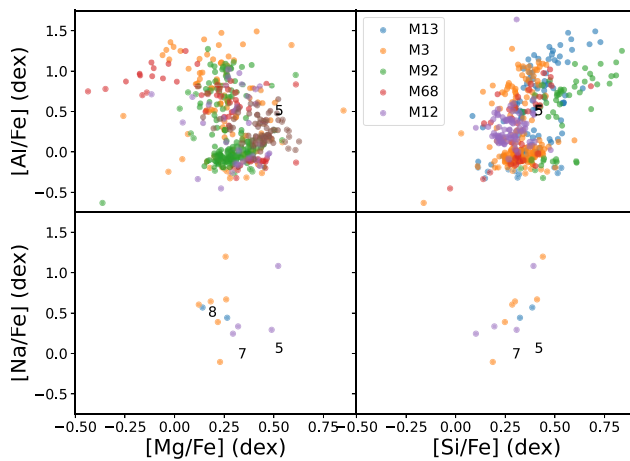


Figure 7. Abundance ratios for the candidate HVSs compared to those known to be observed in globular clusters. Background data are taken from Masseron et al. (2019). If the star lacked 1 of the measurements in a given panel it was excluded from that panel.

7.1 Possible origins for unbound or marginally bound Stars 5, 7, and 8

7.1.1 Globular clusters

We plotted our stars against known abundance trends for globular clusters (see e.g. fig. 2 in Gratton et al. 2019). Due to SNR and weakness of the Al features we had available, we were only able to measure Al for Star 5. All of the stars had abundances within the range seen for a few globular clusters studied in detail from Masseron et al. (2019) and Mészáros et al. (2020) (M13, M3, M92, M68, and M12). We found that none of our stars were enhanced in Al while simultaneously being depleted in Mg, thus are not consistent with being second generation globular cluster stars. The abundance plots are shown in Fig. 7.

Cabrera & Rodriguez (2023) provide 50 per cent and 90 per cent credible phase space regions for stars dynamically ejected out of 148 globular clusters in the MW. For Stars 7 and 8, we find no suitable clusters. Star 5 is at a much greater distance and therefore the proper motion and sky locations are not as constraining on this star's origins. However, based on the second kinematic analysis, it could be plausible for Star 8 to originate from NGC 5897. There is some probability based on the Cabrera & Rodriguez (2023) models for Star 8 to be located in its present region. Star 8 also has a chemical make up which agrees well with the previous characterization of NGC 5897 from Koch & McWilliam (2014). Koch & McWilliam (2014) measure a metallicity of ~ -2.04 and $\alpha/\text{Fe} \sim 0.34$ based on 7 stars from the cluster. We measure Star 8 with a metallicity of ~ -1.97 and $\alpha/\text{Fe} \sim 0.33$, which are within the measurement errors. This conclusion is hampered by our [Na/Fe] measurement which is ~ 0.7 compared to their highest value of ~ 0.6 . They note that NLTE corrections at these parameter ranges might account for a difference of -0.05 dex. Higher SNR follow-up observations of Star 8 would be useful to confirm this possible origin. These observations would also be useful for measuring more elements useful for studying populations of stars in globular clusters (e.g. O, Si, and Al).

7.1.2 LMC

There is interest in detecting HVSs from the LMC, which could offer indirect evidence for the existence of a massive black hole in

the centre of the LMC (Edelmann et al. 2005). Boubert & Evans (2016) provide on sky distributions for LMC stars ejected through the Hills' mechanism and Boubert et al. (2017) create phase space distributions for LMC run away stars. Our on sky distribution of stars is in the lowest or second lowest density contours for both scenarios.

As pointed out in Reggiani et al. (2022), due to the lack of LMC stars over the metallicity range covered by our objects, ruling out these stars came from the LMC based on chemistry alone is difficult. However, we see no positive evidence (i.e. the chemical patterns are not consistent with LMC origins) favouring the LMC over the stellar halo based on chemical abundances.

7.1.3 Low α halo or accreted system

As discussed in Section 6.6, there are no stars in our sample that appeared to simultaneously satisfy the Toomre clustering, $[\alpha/\text{Fe}] \gtrsim 0.3$, and [Na/Fe] versus $[\text{Na}/\text{Fe}]$ grouping that Nissen & Schuster (2010) found for the low α halo. Star 8 appears to have a lower $[\alpha/\text{Fe}]$ value but has very high [Na/Fe] and [Ni/Fe] making it incompatible with the Nissen & Schuster (2010) low α halo origin. Therefore, we can rule out accretion as an origin for these HVSs. We can also rule out origins from a satellite galaxy with Fornax like chemistry due to the disagreements in [Na/Fe] seen in Fig. 5 and the $[\alpha/\text{Fe}]$ seen in Fig. 4.

7.1.4 Galactic centre

Boubert & Evans (2016) provide an on sky distribution for stars ejected from the GC. Our stars fall outside the main density contours of this figure. This is supported by our orbit integration that finds Stars 5, 7, and 8 have not originated within 7 kpc of the GC.

7.1.5 Star 7

This star has been previously found to be likely unbound and characterized in Bromley et al. (2018) and Du et al. (2018) in accord with our result; however, there is disagreement over the origin. Du et al. (2018), using LAMOST (Large Sky Area Multi-Object Fiber Spectroscopic Telescope) abundances, finds an $[\alpha/\text{Fe}]$ of ~ 0.3 which they use as evidence for this star having an accreted origin. We find $[\alpha/\text{Fe}] \sim 0.4$, typical of the stellar halo. Caution should be exercised when comparing these measurements in detail. The line selection, or region selection used in Du et al. (2018) differs from ours as we do not include Ti in our measurements. Bromley et al. (2018) use orbit integration to conclude this star may come from the LMC. While we are able to replicate the timing they give for the disc crossing, we do not find a similar result for the LMC close approach. We find no clear dynamical progenitor for this star and conclude it was likely born in the ‘*in situ*’ stellar halo.

8 SUMMARY

HVSs are rare and useful objects to study both due to their unclear origin and potential applications for the understanding of the Galaxy. While first discovered by Brown et al. (2005), the subfield has seen rapid growth fueled by renewed interest and large-scale surveys, in particular the *Gaia* mission. Brown (2015) estimated a total of 20 confirmed HVS stars, and Boubert et al. (2018) find ~ 500 candidate HVSs. Boubert et al. (2018) found only 1 of the likely unbound HVS candidates was a late-type star.

In this context, we aim to (1) confirm (or not) the HVS status of 16 candidate HVSs taken from the literature, (2) derive their chemical abundance pattern, (3) derive their dynamical properties, and use these pieces of information to (4) constrain their origins. We perform follow-up observations of 16 candidate HVSs based on the literature to confirm their RVs and measure their chemical abundances. We used a combination of the TS on the 2.7-m HJST Telescope at the McDonald observatory and the ARCES spectrograph on the 3.5-m APO telescope. We find good agreement between the RV measurements from *Gaia* and our ground-based observations.

We use the full 6D kinematic information to assess whether these extreme velocity stars are likely unbound or not on the basis of the MW escape velocity model from Williams et al. (2017). We confirm one star (*Gaia* DR3 source id 1383279090527227264) is very likely unbound, and find 2 (*Gaia* DR3 source id 1396963577886583296 and *Gaia* DR3 source id 1478837543019912064) which might be marginally bound (with the details depending on the exact model of the local escape speed used). The remainder appear HiVel (with $v_{\text{total}} > 300 \text{ km s}^{-1}$, and all but one with $v_{\text{total}} > 350 \text{ km s}^{-1}$) but bound. We use orbit integration to search for a possible dynamic origin of these stars. Between the orbital trajectories of the (marginally) unbound HVS and known globular clusters (Vasiliev 2019) and satellite galaxies (Fritz et al. 2018), we attempt to determine the progenitor. We find that none of the marginally bound or unbound sources have a clear progenitor.

We measure chemical abundances for up to 22 species. These elements are Mg, Si, Ca, and Ti (α group), Fe, Cr, Ni, Co, Sr, and Mn (Fe-Peak), Na, Al, V, Cu, and Sc (odd-Z group), and Sr, Y, Zr, Ba, La, Nd, and Eu (neutron capture). These elements span the main nucleosynthetic families. We find our sample is largely consistent with the abundance trends for the inner halo (see e.g. Fig. 5). They do not appear to originate from globular clusters, the LMC, or the GC. Unlike Reggiani et al. (2022) and Quispe-Huaynasi et al. (2022) we do not find any stars chemically consistent with the low $[\alpha/\text{Fe}]$ typical of accreted systems. There are three possible causes for this difference: (1) small number statistics/chance, (2) differences in abundance analysis, and (3) differences in target selection of HiVel star candidates. For (1), it is possible with small ($N \sim 10$ –20 stars), that we, by chance sample, different populations of HiVel stars. Additionally, the stellar parameter and abundance analysis methods are different between various literature which could lead to an differences. Finally, the target selection from this study uses a combination of HVS candidates from four sources as described in Section 2.1. Reggiani et al. (2022) also use Hattori et al. (2018) in their initial selection. However, Quispe-Huaynasi et al. (2022) use their own selection process and Reggiani et al. (2022) use Herzog-Arbeitman, Lisanti & Necib (2018) in addition to Hattori et al. (2018).

The lack of accreted stars in our sample is intriguing in light of recent results such as Mackereth & Bovy (2020), which propose the majority (70 per cent) of the halo is accreted. It is possible the *in situ* halo stars we see are formed in the MW and heated from an early accretion event (e.g. Belokurov et al. 2020). A possible origin for these fast moving stars is they are the metal weak tail of the splash distribution. Many of these stars are on retrograde orbits which can be seen in Fig. 6. This agrees with the observation from Belokurov et al. (2020). $[\text{Al}/\text{Fe}]$ has been argued to distinguish between accreted and *in situ* stars (e.g. Hawkins et al. 2015b; Carrillo et al. 2022). On the basis of our high $[\text{Al}/\text{Fe}]$ measurements, it is plausible these stars again formed in the MW, however these observations should be taken with caution. Beyond the difficulties with measuring Al in our moderate SNR sample and the differences in Al measurements between studies we compare our data with other

studies (see Section 6.7), there are also potential problems with comparing IR measurements of Al with optical ones for metal-poor stars (e.g. Carrillo et al. 2022).

To our knowledge, *Gaia* DR3 source id 1383279090527227264 is one of the first late-type HVS with high-resolution spectra and detailed chemical abundances. Our measurements suggest it is a halo star, ruling out several other proposed origin scenarios. Lacking a known progenitor star cluster, we conclude it was likely accelerated from the Galactic halo. *Gaia* DR3 is likely to reveal many new late type HVS candidates for follow-up work.

ACKNOWLEDGEMENTS

TN and KH acknowledge support from the National Science Foundation grant AST-1907417 and AST-2108736 and from the Wootton Center for Astrophysical Plasma Properties funded under the United States Department of Energy collaborative agreement DE-NA0003843. This work was performed in part at the Aspen Center for Physics, which is supported by National Science Foundation grant PHY-1607611. This work was also performed in part at the Simons Foundation Flatiron Institute’s Center for Computational Astrophysics during KH’s tenure as an IDEA Fellow. This project was developed, in part, at the 2022 New York City Gaia Fete, hosted by the Center for Computational Astrophysics of the Flatiron Institute in New York City. Grant information:

Facilities used: Apache Point Observatory, McDonald Observatory, Simbad

Software used: ASTROPY (Astropy Collaboration 2013, 2018), NUMPY (Harris et al. 2020), IPYTHON (Perez & Granger 2007), MATPLOTLIB (Hunter 2007), GALPY (Bovy 2015), SCIPY (Virtanen et al. 2020), PHOTUTILS (Bradley et al. 2020), BACCHUS (Masseron et al. 2016), TOPCAT (Taylor 2005), and ISPEC (Blanco-Cuaresma et al. 2014b).

DATA AVAILABILITY

Measured stellar atmospheric parameters and abundances are available online through the Strasbourg astronomical Data Center (CDS). Literature data were accessed through public archives or online data tables. The public archives used were Pan-STARRS DR1 (<https://catalogs.mast.stsci.edu/panstarrs/>), *Gaia* DR2 and DR3 (<https://gea.esac.esa.int/archive/>), SDSS-IV (<https://skyserver.sdss.org/dr17/>), SkyMapper DR2 (<https://skymapper.anu.edu.au/data-release/dr2/>), AllWISE (<https://wise2.ipac.caltech.edu/docs/release/allwise/>), and 2MASS (<https://www.ipac.caltech.edu/2mass/>). Data for distances were accessed through the CDS (<https://cdsarc.cds.unistra.fr/viz-bin/cat/I/352>). Comparison data samples used in the abundance sections were accessed via the CDS.

REFERENCES

Abadi M. G., Navarro J. F., Steinmetz M., 2009, *ApJ*, 691, L63
 Astropy Collaboration, 2013, *A&A*, 558, A33
 Astropy Collaboration, 2018, *AJ*, 156, 123
 Bailer-Jones C. A. L., Rybizki J., Fouesneau M., Demleitner M., Andrae R., 2021, *AJ*, 161, 147
 Battistini C., Bensby T., 2015, *A&A*, 577, A9
 Battistini C., Bensby T., 2016, *A&A*, 586, A49
 Belokurov V., Sanders J. L., Fattah A., Smith M. C., Deason A. J., Evans N. W., Grand R. J. J., 2020, *MNRAS*, 494, 3880
 Bennett M., Bovy J., 2019, *MNRAS*, 482, 1417
 Bensby T. et al., 2010, *A&A*, 512, A41
 Bensby T., Feltzing S., Oey M. S., 2014, *A&A*, 562, A71

Bergemann M., 2011, *MNRAS*, 413, 2184

Bergemann M., Gehren T., 2008, *A&A*, 492, 823

Bergemann M., Pickering J. C., Gehren T., 2010, *MNRAS*, 401, 1334

Bergemann M., Lind K., Collet R., Magic Z., Asplund M., 2012a, *MNRAS*, 427, 27

Bergemann M., Kudritzki R.-P., Plez B., Davies B., Lind K., Gazak Z., 2012b, *ApJ*, 751, 156

Bergemann M., Kudritzki R.-P., Würl M., Plez B., Davies B., Gazak Z., 2013, *ApJ*, 764, 115

Bergemann M., Kudritzki R.-P., Gazak Z., Davies B., Plez B., 2015, *ApJ*, 804, 113

Bergemann M., Collet R., Amarsi A. M., Kovalev M., Ruchti G., Magic Z., 2017, *ApJ*, 847, 15

Blaauw A., 1961, *Bull. Astron. Inst. Netherlands*, 15, 265

Blanco-Cuaresma S., Soubiran C., Jofré P., Heiter U., 2014a, *A&A*, 566, A98

Blanco-Cuaresma S., Soubiran C., Heiter U., Jofré P., 2014b, *A&A*, 569, A111

Bland-Hawthorn J., Gerhard O., 2016, *ARA&A*, 54, 529

Blanton M. R. et al., 2017, *AJ*, 154, 28

Bochanski J. J., Faherty J. K., Gagné J., Nelson O., Coker K., Smithka I., Desir D., Vasquez C., 2018, *AJ*, 155, 149

Boubert D., Evans N. W., 2016, *ApJ*, 825, L6

Boubert D., Erkal D., Evans N. W., Izzard R. G., 2017, *MNRAS*, 469, 2151

Boubert D., Guillochon J., Hawkins K., Ginsburg I., Evans N. W., Strader J., 2018, *MNRAS*, 479, 2789

Bovy J., 2015, *ApJS*, 216, 29

Bradley L. et al., 2020, astropy/photutils: 1.0.0

Bromley B. C., Kenyon S. J., Brown W. R., Geller M. J., 2018, *ApJ*, 868, 25

Brown W. R., 2015, *ARA&A*, 53, 15

Brown W. R., Geller M. J., Kenyon S. J., Kurtz M. J., 2005, *ApJ*, 622, L33

Brown W. R., Geller M. J., Kenyon S. J., 2014, *ApJ*, 787, 89

Buchner J. et al., 2014, *A&A*, 564, A125

Burbidge E. M., Burbidge G. R., Fowler W. A., Hoyle F., 1957, *Rev. Mod. Phys.*, 29, 547

Cabrera T., Rodriguez C. L., 2023, *ApJ*, 953, 19

Capuzzo-Dolcetta R., Fragione G., 2015, *MNRAS*, 454, 2677

Carrillo A., Hawkins K., Jofré P., de Brito Silva D., Das P., Lucey M., 2022, *MNRAS*, 513, 1557

Cayrel R., 1988, in Cayrel de Strobel G., Spite M. eds, Proc. IAU Symp. 132, The Impact of Very High S/N Spectroscopy on Stellar Physics. Kluwer Academic Publishers, Dordrecht, p. 345

Chambers K. C. et al., 2016, preprint ([arXiv:1612.05560](https://arxiv.org/abs/1612.05560))

Clark J. T. et al., 2022, *MNRAS*, 510, 2041

Coe D., 2009, preprint ([arXiv:0906.4123](https://arxiv.org/abs/0906.4123))

Curtis S., Ebinger K., Fröhlich C., Hempel M., Perego A., Liebendörfer M., Thielemann F.-K., 2019, *ApJ*, 870, 2

Dotter A., 2016, *ApJS*, 222, 8

Drimmel R., Poggio E., 2018, *Res. Notes Am. Astron. Soc.*, 2, 210

Du C., Li H., Newberg H. J., Chen Y., Shi J., Wu Z., Ma J., 2018, *ApJ*, 869, L31

Edelmann H., Napiwotzki R., Heber U., Christlieb N., Reimers D., 2005, *ApJ*, 634, L181

El-Badry K. et al., 2023, *Open J. Astrophys.*, 6, 28

Evans D. W. et al., 2018, *A&A*, 616, A4

Feltzing S., Chiba M., 2013, *New Astron. Rev.*, 57, 80

Frebel A., Casey A. R., Jacobson H. R., Yu Q., 2013, *ApJ*, 769, 57

Freeman K., Bland-Hawthorn J., 2002, *ARA&A*, 40, 487

Fritz T. K., Battaglia G., Pawłowski M. S., Kallivayalil N., van der Marel R., Sohn S. T., Brook C., Besla G., 2018, *A&A*, 619, A103

GRAVITY Collaboration, 2018, *A&A*, 615, L15

Gaia Collaboration, 2016, *A&A*, 595, A1

Gaia Collaboration, 2018, *A&A*, 616, A1

Gaia Collaboration, 2021, *A&A*, 649, A1

Gallo A., Ostorero L., Chakrabarty S. S., Ebagezio S., Diaferio A., 2022, *A&A*, 663, A72

Gilmore G., Wyse R. F. G., Kuijken K., 1989, *ARA&A*, 27, 555

Gnedin O. Y., Gould A., Miralda-Escudé J., Zentner A. R., 2005, *ApJ*, 634, 344

Gonzalez O. A. et al., 2015, *A&A*, 584, A46

Gratton R., Bragaglia A., Carretta E., D’Orazi V., Lucatello S., Sollima A., 2019, *A&AR*, 27, 8

Gray D. F., 2008, The Observation and Analysis of Stellar Photospheres. Cambridge University Press, Cambridge, UK

Green G. M., Schlafly E., Zucker C., Speagle J. S., Finkbeiner D., 2019, *ApJ*, 887, 93

Grevesse N., Asplund M., Sauval A. J., 2007, *Space Sci. Rev.*, 130, 105

Gualandris A., Portegies Zwart S., 2007, *MNRAS*, 376, L29

Gustafsson B., Edvardsson B., Eriksson K., Jørgensen U. G., Nordlund Å., Plez B., 2008, *A&A*, 486, 951

Harris C. R. et al., 2020, *Nature*, 585, 357

Hattori K., Valluri M., Bell E. F., Roederer I. U., 2018, *ApJ*, 866, 121

Hawkins K., Wyse R. F. G., 2018, *MNRAS*, 481, 1028

Hawkins K. et al., 2015a, *MNRAS*, 447, 2046

Hawkins K., Jofré P., Masseron T., Gilmore G., 2015b, *MNRAS*, 453, 758

Hawkins K. et al., 2020a, *MNRAS*, 492, 1164

Hawkins K., Lucey M., Curtis J., 2020b, *MNRAS*, 496, 2422

Heber U., Edelmann H., Napiwotzki R., Altmann M., Scholz R. D., 2008, *A&A*, 483, L21

Heiter U., Jofré P., Gustafsson B., Korn A. J., Soubiran C., Thévenin F., 2015, *A&A*, 582, A49

Heiter U. et al., 2021, *A&A*, 645

Helmi A., Babusiaux C., Koppelman H. H., Massari D., Veljanoski J., Brown A. G. A., 2018, *Nature*, 563, 85

Herzog-Arbeitman J., Lisanti M., Necib L., 2018, *J. Cosmol. Astropart. Phys.*, 2018, 052

Hills J. G., 1988, *Nature*, 331, 687

Hunter J. D., 2007, *Comput. Sci. Eng.*, 9, 90

Igoshev A. P., Perets H., Hallakoun N., 2023, *MNRAS*, 518, 6223

Ji A. P. et al., 2020, *AJ*, 160, 181

Jofré P. et al., 2014, *A&A*, 564, A133

Jofré P. et al., 2017, *A&A*, 601, A38

Kenyon S. J., Bromley B. C., Geller M. J., Brown W. R., 2008, *ApJ*, 680, 312

Kenyon S. J., Bromley B. C., Brown W. R., Geller M. J., 2018, *ApJ*, 864, 130

Kirby E. N., Guhathakurta P., Bolte M., Sneden C., Geha M. C., 2009, *ApJ*, 705, 328

Kobayashi C., Karakas A. I., Lugaro M., 2020, *ApJ*, 900, 179

Koch A., McWilliam A., 2014, *A&A*, 565, A23

Korn A. J., Shi J., Gehren T., 2003, *A&A*, 407, 691

Kroupa P., Weidner C., 2003, *ApJ*, 598, 1076

Kurucz R. L., 1992, *Rev. Mex. Astron. Astrofis.*, 23, 45

Lambert D. L., 1987, *J. Astrophys. Astron.*, 8, 103

Leonard P. J. T., Duncan M. J., 1988, *AJ*, 96, 222

Letarte B. et al., 2010, *A&A*, 523, A17

Li Y.-B. et al., 2021, *ApJS*, 252, 3

Mackereth J. T., Bovy J., 2020, *MNRAS*, 492, 3631

Magnier E. A. et al., 2020, *ApJS*, 251, 6

Majewski S. R. et al., 2017, *AJ*, 154, 94

Marchetti T., 2021, *MNRAS*, 503, 1374

Marchetti T., Rossi E. M., Brown A. G. A., 2019, *MNRAS*, 490, 157

Marchetti T., Evans F. A., Rossi E. M., 2022, *MNRAS*, 515, 767

Mashonkina L., Korn A. J., Przybilla N., 2007, *A&A*, 461, 261

Masseron T. et al., 2014, *A&A*, 571, A47

Masseron T., Merle T., Hawkins K., 2016, Astrophysics Source Code Library, record ascl:1605.004

Masseron T. et al., 2019, *A&A*, 622, A191

Mészáros S. et al., 2020, *MNRAS*, 492, 1641

Miyamoto M., Nagai R., 1975, *PASJ*, 27, 533

Mucciarelli A., Bonifacio P., 2020, *A&A*, 640, A87

Navarro J. F., Frenk C. S., White S. D. M., 1996, *ApJ*, 462, 563

Nelson T., Ting Y.-S., Hawkins K., Ji A., Kamdar H., El-Badry K., 2021, *ApJ*, 921, 118

Nissen P. E., Schuster W. J., 2010, *A&A*, 511, L10

Nomoto K., Kobayashi C., Tominaga N., 2013, *ARA&A*, 51, 457

Pereira C. B., Jilinski E., Drake N. A., de Castro D. B., Ortega V. G., Chavero C., Roig F., 2012, *A&A*, 543, A58

Perets H. B., Wu X., Zhao H. S., Famaey B., Gentile G., Alexander T., 2009, *ApJ*, 697, 2096

Perez F., Granger B. E., 2007, *Comput. Sci. Eng.*, 9, 21

Piffl T. et al., 2014, *A&A*, 562, A91

Plez B., 2012, Astrophysics Source Code Library, record ascl:1205.004

Poveda A., Ruiz J., Allen C., 1967, Bol. Obs. Tonantzintla Tacubaya, 4, 86

Quispe-Huaynasi F. et al., 2022, *AJ*, 164, 187

Radzi R., Irrgang A., Heber U., Schneider D., Kreuzer S., 2021, *A&A*, 645, A108

Reggiani H., Ji A. P., Schlaufman K. C., Frebel A., Necib L., Nelson T., Hawkins K., Galarza J. Y., 2022, *AJ*, 163, 252

Reid M. J., Brunthaler A., 2004, *ApJ*, 616, 872

Roederer I. U., Preston G. W., Thompson I. B., Shectman S. A., Sneden C., Burley G. S., Kelson D. D., 2014, *AJ*, 147, 136

Rossi E. M., Marchetti T., Cacciato M., Kuiack M., Sari R., 2017, *MNRAS*, 467, 1844

Sesana A., Haardt F., Madau P., 2007, *MNRAS*, 379, L45

Shen K. J. et al., 2018, *ApJ*, 865, 15

Skrutskie M. F. et al., 2006, *AJ*, 131, 1163

Steinmetz M. et al., 2006, *AJ*, 132, 1645

Taylor M. B., 2005, in Shopbell P., Britton M., Ebert R.eds, ASP Conf. Ser. Vol. 347, Astronomical Data Analysis Software and Systems XIV. Astron. Soc. Pac., San Francisco, p. 29

Ting Y.-S., Conroy C., Rix H.-W., Cargile P., 2019, *ApJ*, 879, 69

Tull R. G., MacQueen P. J., Sneden C., Lambert D. L., 1995, *PASP*, 107, 251

Tutukov A. V., Fedorova A. V., 2009, *Astron. Rep.*, 53, 839

Van der Swaelmen M., Hill V., Primas F., Cole A. A., 2013, *A&A*, 560, A44

Vasiliev E., 2019, *MNRAS*, 484, 2832

Virtanen P. et al., 2020, *Nat. Methods*, 17, 261

Wang S.-I. et al., 2003, in Iye M., Moorwood A. F. M.eds, Proc. SPIE Conf. Ser. Vol. 4841, Instrument Design and Performance for Optical/Infrared Ground-based Telescopes. SPIE, Bellingham, p. 1145

Weinberg D. H. et al., 2019, *ApJ*, 874, 102

Wheeler J. C., Sneden C., Truran James W. J., 1989, *ARA&A*, 27, 279

Williams A. A., Belokurov V., Casey A. R., Evans N. W., 2017, *MNRAS*, 468, 2359

Wolf C. et al., 2018, *Publ. Astron. Soc. Aust.*, 35, e010

Wright E. L. et al., 2010, *AJ*, 140, 1868

Yong D. et al., 2013, *ApJ*, 762, 26

York D. G. et al., 2000, *AJ*, 120, 1579

Yu Q., Tremaine S., 2003, *ApJ*, 599, 1129

van de Voort F., Pakmor R., Grand R. J. J., Springel V., Gómez F. A., Marinacci F., 2020, *MNRAS*, 494, 4867

SUPPORTING INFORMATION

Supplementary data are available at [MNRAS](https://mnras.oxfordjournals.org) online.

suppl_data

Please note: Oxford University Press is not responsible for the content or functionality of any supporting materials supplied by the authors. Any queries (other than missing material) should be directed to the corresponding author for the article.

APPENDIX A: ADQL QUERY FOR STARS 15 AND 16

The query used to find two candidate HVS stars targeted for follow-up observations in this work. The cuts are based on high RV in the galactocentric rest frame.

```
SELECT *
  FROM gaiadr3.gaia_source
 WHERE parallax_error/parallax <= 0.1
   AND abs(radial_velocity + 8.5*cos
          (RADIANS(1))*cos(RADIANS(b)) +
          233.38*sin(RADIANS(1))*cos(RADIANS(b)))
          + 6.49*sin(RADIANS(b))) >= 400
   AND pmra_error < 1
   AND pmdec_error < 1
   AND radial_velocity_error < 5
   AND parallax > 0
```

This paper has been typeset from a *T_EX/L_AT_EX* file prepared by the author.